



Skolkovo Institute of Science and Technology

MASTER'S THESIS

**DFT study of hydroxyl defects
in LiFePO₄ and LiMnPO₄ cathode materials**

Master's Educational Program: 22.04.01 Materials Science and Engineering

Student _____

Irina Varlamova

Research Advisor: _____

Andriy Zhugayevych
Assistant Professor

Co-Advisor: _____

Dmitry Aksenov
Senior Research Scientist

Moscow 2020

All rights reserved. ©

The author hereby grants to Skoltech permission to reproduce and to distribute publicly paper and electronic copies of this thesis document in whole and in part in any medium now known or hereafter created.



Skolkovo Institute of Science and Technology

МАГИСТЕРСКАЯ ДИССЕРТАЦИЯ

**Исследование гидроксильных дефектов в катодных
материалах LiFePO₄ и LiMnPO₄ с помощью метода DFT**

Магистерская образовательная программа:
22.04.01 Материаловедение и технологии материалов

Студент _____
Ирина Варламова

Научный руководитель:_____
Андрей Жугаевич
Старший Преподаватель

Со-руководитель:_____
Дмитрий Аксёнов
Старший научный сотрудник

Москва 2020
Все права защищены.©

Автор настоящим дает Сколковскому институту науки и технологий разрешение на воспроизведение
и свободное распространение бумажных и электронных копий настоящей диссертации в целом или
частично на любом ныне существующем или созданном в будущем носителе.

**DFT study of hydroxyl defects
in LiFePO₄ and LiMnPO₄ cathode materials**

Irina Varlamova

Submitted to the Skolkovo Institute of Science and Technology
on 29 May, 2020

ABSTRACT

The transition to all-electric vehicles (EV) and renewable energy heavily relies on the further development of Li-ion batteries. One of the most prospective Li-ion technology is based on LiFePO₄ cathode material, which combines high stability, safety, and affordability. However, the further improvement of this material, including full or partial replacement of Fe by Mn for an increase of voltage, requires better understanding and control of residual point defects left after synthesis.

Recently, it is shown experimentally, that hydrothermally synthesized LiFePO₄ cathode material can contain previously unknown OH-type defects, which have a detrimental effect on electrochemical properties. However, the direct observation of OH defect atomic structure was proved to be highly challenging with experimental techniques. Therefore, in the current work to overcome experimental difficulties we employ computational methods based on density functional theory to study the energetics and structure of OH defects in LiFePO₄ and LiMnPO₄ cathode compounds.

We consider all possible OH defects, where H resides either in interstitial voids or substitute Li, Fe, or P. The calculation of defects formation energies shows that PO₄/(OH)₄ substitution is the most favorable among considered defects, explaining experimental results. By performing a full potential energy surface scan it is found that the atomic structure of PO₄/(OH)₄ defect is similar to the hydrogarnet defect observed in silicon-based minerals. Finally, the dynamics of this defect is studied at elevated temperatures with *ab initio* molecular dynamics.

Research Advisor:

Name: Andriy Zhugayevych

Degree: Candidate of Science degree in Physics and Mathematics

Title: Assistant Professor

Co-Advisor:

Name: Dmitry Aksenov

Degree: Candidate of Sciences degree in Physics and Mathematics

Title: Senior Research Scientist

Acknowledgments

I would like to express my sincere gratitude to my advisors Snr.Research Scientist Dmitry Aksenov and Prof.Andriy Zhugayevych for the continuous support of my study in the master's degree program and related research, for their patience, motivation, and immense knowledge. Their guidance helped me in all the time of research and writing of this thesis. I would particularly like to thank Dmitry Aksenov for his assistance in making the necessary calculations with Hubbard correction. Thank you to my supervisor,Andriy Zhugayevych, for his help with molecular dynamics analysis.

My sincere thanks also go to Dr.Tejs Vegge, Prof.Jinhyun Chang, and Prof.Juan Maria García Lastra of Denmark Technical University (DTU), who provided me an opportunity to join their team as an intern, and who gave access to the high-performance calculation cluster Niflheim and research facilities.

Contents

Introduction	7
1 Review of Literature	9
1.1 Comparison of different battery systems and cathode materials	9
1.2 Crystal structure of LiFePO ₄ and LiMnPO ₄ material	11
1.3 Synthesis method for LiFePO ₄ cathode material	12
1.4 Electronic structure of LiFePO ₄ and LiMnPO ₄	13
1.5 Defects in LiFePO ₄ and LiMnPO ₄ cathode materials	14
1.6 OH defects in olivine (Mg, Fe)SiO ₄ minerals	15
2 Methodology	17
2.1 Density Functional Theory key concepts	17
2.2 Computational details	19
2.3 Scan of hydrogen potential energy surface	19
2.4 Molecular Dynamics study	20
3 Results	21
3.1 Calculation of bulk properties	21
3.2 Structure and energetics of H interstitial and Li/H and Fe/2H substitution defects .	22
3.3 Potential energy surface of four H atoms in P vacancy	28
3.3.1 PES for PO ₄ /O ₄ H ₁ defect	29
3.3.2 PES for PO ₄ /O ₄ H ₂ defect	32
3.3.3 PES for PO ₄ /O ₄ H ₃ defect	34
3.3.4 PES for PO ₄ /(OH) ₄	36
3.4 Formation energy of OH defects in LiFePO ₄	38
3.5 Molecular dynamic simulation	39
3.6 Structure of PO ₄ /(OH) ₄ defect in LiFePO ₄ and LiMnPO ₄	42
3.7 Electronic properties of defective structures	43
3.8 Discussion	46
Conclusions	47

A Program code	48
A.1 Potential Energy Surface method	48
A.2 Solution energies calculation	49
A.3 Juxtaposition between color and energy of each hydrogen position	50
A.4 To reduce the extreme energy values	51
A.5 To create the jmol script to visualize the full hydrogen distribution	52

Introduction

The transition to sustainable energy, established on renewables and electric transport, critically depends on the development of efficient and affordable energy storage devices - rechargeable batteries. Among existing battery technologies Li-ion possesses many advantages in terms of specific energy, longevity, and power rate, explaining its fast penetration into portable electronics, electric cars, and even grid storage. One of the most prospective Li-ion technology is based on LiFePO_4 cathode material, which combines high stability, safety, and affordability. However, the further improvement of this material, including full or partial replacement of Fe by Mn for an increase of voltage, requires better understanding and control of residual point defects left after synthesis. Recently, it is shown with powder X-ray (PXRD) and neutron diffraction analysis, that hydrothermally synthesized LiFePO_4 (LFP) cathode material can have a deficiency in phosphorus, which should be highly unfavorable from the thermodynamic point of view [1]. By careful analysis of iron oxidation states, Sumanov et al. suggested that some compensation mechanism should exist in P deficient LFP material. The infrared spectroscopy showed peaks from structural OH bonds, while thermogravimetric/mass-spectrometry analysis revealed the water loss by LFP sample in two stages with onsets at 350 and 450 °C. Based on these results it was concluded that the compensation mechanism is related to the formation of structural OH defects, which can stabilize P vacancies. It was confirmed that the structural OH defects are not completely eliminated even up to 650 °C. Sumanov et al. provided density functional calculations for $\text{PO}_4/(\text{OH})_4$ substitutional defect, however they did not consider other possibilities for hydrogen insertions and substitutions. Therefore, the structure and energetics of OH-defects in LiFePO_4 material remain unclear. The complexity of the task is related to several degrees of freedom in $\text{PO}_4/(\text{OH})_3$ and $\text{PO}_4/(\text{OH})_4$ defects, which can result in numerous metastable configurations. Hence, the computational study of these defects should include global minima search approaches such as potential energy surface scan, while the defect stability should be studied with molecular dynamics at elevated temperatures.

The main aim of the current work is to determine the structure and energetics of OH defects in $\text{Li}(\text{Fe,Mn})\text{PO}_4$ compounds using computational tools based on density functional theory.

To achieve the aim we set the following tasks:

1. Calculate the energy and structure of OH defects in tetrahedral and octahedral voids of LiFePO_4 ;
2. Calculate the energy and structure of Li/H and Fe/2H substitution defects in LiFePO_4 ;

3. Construct full potential energy surface for $\text{PO}_4/(\text{OH})_4$ substitution defect and calculate its formation energy and structure in $\text{Li}(\text{Fe,Mn})\text{PO}_4$;
4. Study the dynamics and stability of $\text{PO}_4/(\text{OH})_4$ defects in LiFePO_4 at elevated temperatures with ab initio molecular dynamics.

Chapter 1

Review of Literature

1.1 Comparison of different battery systems and cathode materials

An electric battery is one of the most important parts of modern electronic devices for everyday use. There are two types of batteries: primary and secondary batteries. The first one is non-rechargeable and is discarded after single-use. In some cases such batteries are appropriate, for example in low-consuming electronics such as arm watches, where one battery can work for several years. However, in many cases primary batteries are still used in relatively high-power applications. The well-known example of high-load primary battery is an alkaline AA cell. It has a relatively small capacity of 700 mAh, and a low voltage of 1.5 V [2]. The energy required to produce the battery is about 50 times greater than the battery stores itself. Moreover, such batteries are environmentally unfriendly. Therefore, whenever possible the primary batteries should be replaced with rechargeable analogs.

There are several types of secondary batteries, like lead-acid, nickel-cadmium (Ni-Cd), nickel-metal hydride (Ni-MH), nickel-iron (Ni-Fe) and lithium-ion (Li-ion) battery. While every technology has its unique niche applications, the Li-ion has the highest energy density and the best longevity among them. As a result of that, several years ago Li-ion has become the only choice for smartphones and laptops, while becoming now to be the most popular energy storage technology in electric cars and even smart grids.

The main components of a Li-ion battery are anode (a negative electrode with oxidation reaction), a cathode (a positive electrode with reduction reaction) and electronically non-conductive electrolyte. There is a lot of research related to the development of these components [3, 4]. Below we focus on materials used for Li-ion cathode production.

Several different materials are used as cathodes in Li-ion batteries. One of the most successful commercial cathode material is LiCoO_2 and was introduced in 1990. This material has high voltage and high theoretical capacity of 274 mAhg^{-1} ; however the latter is reduced to the practical values of $140\text{-}160 \text{ mAhg}^{-1}$ [5]. To achieve higher capacities, charging above 4.2V is required, which results in phase transformations from the hexagonal ($\text{R}\bar{3}\text{m}$) to the monoclinic structure, oxy-

gen release and corresponding fast degradation [6]. Overall, stability of the material is poor and thermal runaway is possible. Additionally, cobalt is quite expensive and its manufacture and recycling is environmentally unfriendly.

To achieve better parameters, several materials were identified as prospective cathodes: LiNiO_2 , LiMn_2O_4 , LiV_3O_8 , LiMPO_4 ($\text{M} = \text{Fe}, \text{Mn}, \text{Co}$) and solid solutions like $\text{LiNi}_{x}\text{Co}_{y}\text{Mn}_{z}\text{O}_2$. For example LiNiO_2 has hexagonal structure $\bar{\text{R}}\bar{3}\text{m}$, it provides practical capacity up to 200 mAhg^{-1} at working voltage more than 4.8 V vs. Li^+/Li [7]. Additionally, such a cathode is less toxic and has a lower price compared to LiCoO_2 . However, LiNiO_2 has the problems related to synthesis, safety and irreversible phase transformation. Another possible material is high-rate LiMn_2O_4 with spinel structure, which is less toxic and more economically favorable in comparison with LiCoO_2 [8]. But due to its lower capacity (120 mAhg^{-1}) and limited life circle it does not correspond to modern requirements as well.

The solid solutions such as $\text{LiNi}_{x}\text{Co}_{y}\text{Mn}_{z}\text{O}_2$ can combine the advantages of single transition metal oxides described above. Such materials demonstrate practical capacities up to 220 mAhg^{-1} and very good capacity retention up to 5000 cycles [9]. However, such materials still have relatively high prices and reduced thermal stability [10].

Alternative oxide cathode materials are lithium trivanadate LiV_3O_8 (and other vanadium oxides), which has a high theoretical capacity (approximately 226 mAhg^{-1} [11]), relativity low cost and long life cycle. However low voltage of vanadium oxides prohibited their commercialization [12].

One of the most economically viable material is LiFePO_4 , which is based on the most abundant and cheap transition metal. This material was discovered in 1997 by Padhi et al. [13]. According to Padhi et al. and numerous following researches LiFePO_4 shows several advantages in comparison with oxide cathode materials. Firstly, LiFePO_4 has low toxicity and cheap due to the abundance of iron. Secondly, LiFePO_4 has higher thermal stability in a charged state with respect to phase transformations and oxygen evolution. Thirdly, it shows excellent cycling stability. The main disadvantage of LiFePO_4 is poor electronic conductivity, which is, however, solved by mixing with conductive carbon additive. Despite lower working voltage and capacity of LiFePO_4 compare to oxides, it has been commercialized and found application in electric buses and energy storage systems. The practical specific capacity, which is close to theoretical (till 170 mAhg^{-1}), combined with operating voltage of 3.5V gives practical specific energies up to 580 Whkg^{-1} [14].

LiMnPO_4 has the same crystal structure and specific capacity as LiFePO_4 , but posses a higher voltage of 4.1 eV vs. Li^+/Li , which gives a higher specific energy of 701 Whkg^{-1} [15]. However, LiMnPO_4 is less stable then LiFePO_4 and suffers from structure disordering during cycling due to the Jahn-Teller effect. Also, LiMnPO_4 has slower ionic kinetics than LiFePO_4 [16]. Besides that, there are numerous efforts [17, 18] to overcome these limitations and create a new

generation of cathodes based on LiMnPO₄ material.

1.2 Crystal structure of LiFePO₄ and LiMnPO₄ material

LiFePO₄, found in nature as triphyllite mineral, has a crystal structure with *Pnma* space group. This crystal structure is well known from studies on olivine minerals (Mg₂SiO₄) - widely present in Earth's mantle. Its framework consists of a slightly distorted hexagonal close-packed anion lattice with half of the octahedral sites occupied with Li and Fe and one-eighth of tetrahedral sites occupied by P. The lithium ions occupy the octahedral sites M₁ forming the edge-shared chains along the c-axes(Figure 1.1 a)). The PO₄ tetrahedron makes the whole framework rigid allowing Li deintercalation. The iron (or magnesium) atoms localize in zigzag chains of corner-shared octahedral sites M₂ parallel to the c-axes (Figure 1.1 a)). The unit cell of LiFePO₄ and LiMnPO₄ is presented in Figure 1.1 b). The experimental lattice constants for LiFePO₄ measured at 293K temperature have the following values: a = 10.32 Å, b = 6.01 Å, and c = 4.69 Å [19]. The lattice constants of LiMnPO₄ are: a = 10.445 Å, b = 6.10 Å, and c = 4.74 Å [19].

According to DFT calculations the barrier for Li vacancy migration along [010] direction is 0.3 eV [20]. The migration pathway between adjacent lithium sites has a nonlinear curved shape. The same diffusion channels and pathway shape is observed for Li migration in LiMnPO₄, but the rate capability is lower due to higher Li vacancy - small polaron complexes formation energy and higher small polaron migration barriers [21].

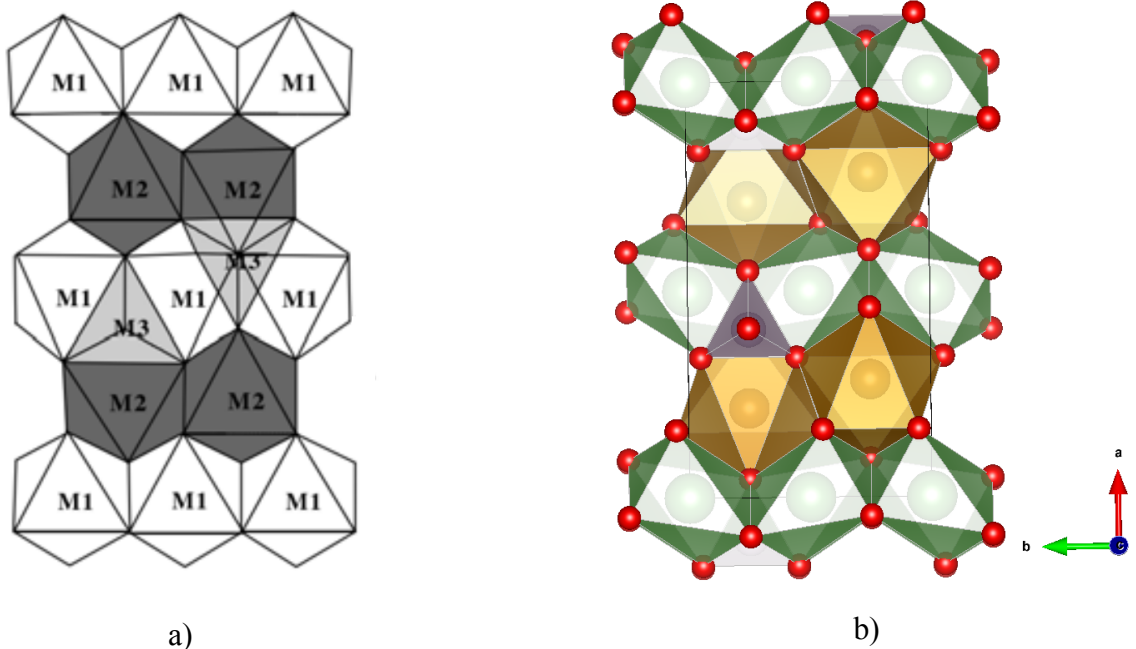


Figure 1.1: Crystal structure of Li(Fe,Mn)PO₄ (a) ideal model; (b) schematic unit cell

The main advantage of LiFe(Mn)PO₄ crystal structure is its thermodynamic and thermal

stability even at temperatures above 200°C due to the strong P-O covalent bonds. The $(\text{PO}_4)^{3-}$ complexes are isolated from each other and touch the Fe octahedrons by sharing one of their edges. The deintercalation of Li^+ ions involves the change of iron oxidation states from Fe^{2+} to Fe^{3+} (or from Mn^{2+} to Mn^{3+} for LiMnPO_4) during the charge process without structural distortion. Since the energy level of $\text{Fe}^{2+}/\text{Fe}^{3+}$ redox couple lies lower by 3.5 eV with respect to the Fermi level of lithium (Figure 1.2), LiMnPO_4 based battery provides the operating voltage of 3.5 V versus Li/Li^+ . In the case of LiMnPO_4 the working voltage is equal to 4.1 V [22].

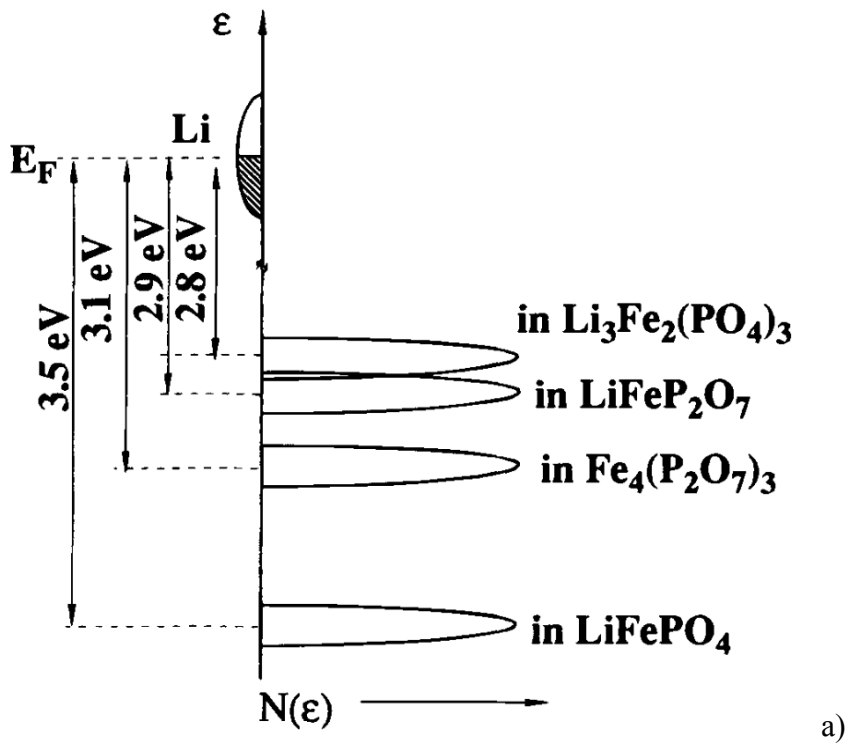


Figure 1.2: Relative energy of $\text{Fe}^{2+}/\text{Fe}^{3+}$ redox couple in LiFePO_4 [13]

1.3 Synthesis method for LiFePO_4 cathode material

The material of $\text{Li}(\text{Fe,Mn})\text{PO}_4$ can be produced using several synthesis methods [23]. These include high-temperature solid-state method, sol-gel method, hydrothermal method and others. However, $\text{Li}(\text{Fe,Mn})\text{PO}_4$ has low electric conductivity and relatively slow lithium-ion diffusion [13], it is necessary to control the particle size during the synthesis process to shorten the [010] diffusion path for Li^+ ion and, thus, to improve the rate capability of $\text{Li}(\text{Fe,Mn})\text{PO}_4$ [24]. Additionally, highly dispersed carbonaceous materials can be added to $\text{Li}(\text{Fe,Mn})\text{PO}_4$ in order to increase its electronic conductivity. The electrochemical activity of $\text{Li}(\text{Fe,Mn})\text{PO}_4$ is strongly dependent on the preparation method. The hydrothermal method gives materials with high electrochemical properties, furthermore, it is simpler in use and energetically more efficient in comparison with

alternative methods. Particles of LiFePO_4 are prepared by hydrothermal reaction from weak precursor solutions: LiOH , FeSO_4 and $(\text{NH}_4)_3\text{PO}_4$ in a molar ratio of 3:1:1. Precursors for LiMnPO_4 material synthesis are: Li_2SO_4 , MnSO_4 and $\text{NH}_4\text{H}_2\text{PO}_4$, with a molar ratio of 3:1:1. After solutions mixing and heating in the Ar-atmosphere in autoclave at 230°C the resultant precipitation is collected and washed by water with ethanol and dried at 80°C in vacuum. The post-annealing process is necessary to perform at a high temperature above 500°C for 1 hour in order to achieve the crystallinity and enhance the electrochemical reactivity [25].

1.4 Electronic structure of LiFePO_4 and LiMnPO_4

Due to low electric conductivity of LiFePO_4 it took more than 10 years to switch from research to the commercial production of cathodes. According to DFT calculations [26], the energy gaps for LiFePO_4 and FePO_4 are 3.7 eV and 1.9 eV, respectively, Figure 1.3. The total density of states provided in this figure shows that the top of the valence band and bottom of the conduction band are occupied by electrons with the minority and majority spin channels, respectively.

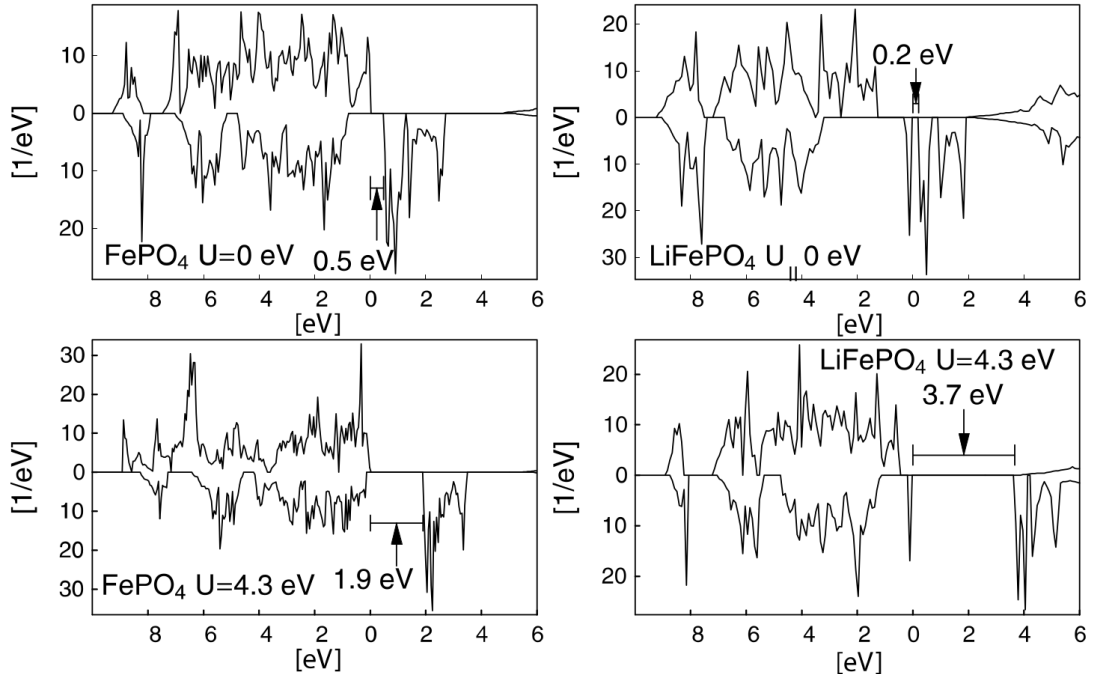


Figure 1.3: Density of states of LiFePO_4 and FePO_4 in GGA and GGA+U methods

The Hubbard correction increases band gap of LiFePO_4 up to 3.7 eV, which is in good alignment with experimental results [26]. The band gap for LiMnPO_4 is 3.8 eV (Figure 1.4), which is also in good agreement with the experiment [27]. Therefore, the correct description of electronic structure requires to use DFT+U method.

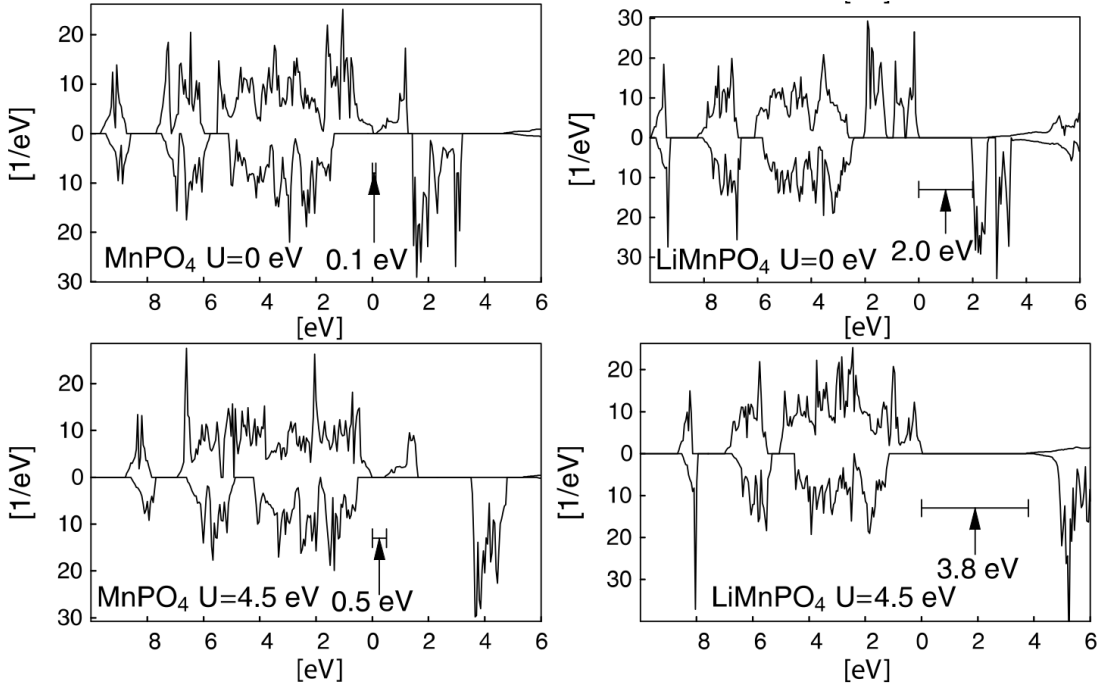


Figure 1.4: Density of states of LiMnPO_4 and MnPO_4 in GGA and GGA+U methods

1.5 Defects in LiFePO_4 and LiMnPO_4 cathode materials

Though LiFePO_4 and LiMnPO_4 materials have a fairly simple crystal structure compared to other polyanionic compounds, investigation of defects in it is still a very important and active topic. The defects can have a huge influence on the electrochemical performance of the battery as a whole, and their study is critical for further material improvement. In literature, the majority of defect studies were conducted for LiFePO_4 rather than for LiMnPO_4 . Below we provide a short review of the obtained results.

The antisite Li-Fe pair is an ‘intersite exchange’ point defect, which is the most abundant point defect in LiFePO_4 material [28]. Islam et al. studied such antisite defects using classical potentials and confirmed that among possible point defects it has the lowest formation energy [28]. The reason for low formation energy of antisite is related to close ionic radii of cations (0.76 Å for Li^+ and 0.78 Å for Fe^{2+}) and corresponding M-O distances. Indeed, the Fe-O and Li-O distances in LiFePO_4 are 2.150 Å and 2.156 Å, respectively. The antisite defect pairs $\text{Fe}_{\text{Li}}^{\bullet} - \text{Li}_{\text{Fe}}^{\circ}$ were directly observed in the experimental study with transmission electron microscopy blue (check) [29, 30] and was identified in diffraction studies [31]. Using DFT calculations the aggregation of Li-Fe antisite pairs was established for LiFePO_4 , while no aggregation was found in LiMnPO_4 [32].

It is considered that antisite defects reduce ionic conductivity of $\text{Li}(\text{Fe,Mn})\text{PO}_4$ by blocking Li^+ [010] diffusion channels by Fe^{2+} or Mn^{2+} cations. Also, part of Li^+ is becoming electrochemically inactive, which reduces specific capacity of material. To reduce the amount of Li-Fe antisite defects the special measures are undertaken during the synthesis. In particular, a post-heat treat-

ment at 500°C [33] results in defects recombination. Also, it is shown that nanosized powder of LFP contains less amount of antisite defects [34].

The removal of one Li results in a negatively charged V_{Li}^+ , which is compensated by the change of the Fe oxidation state from +2 to +3 with the formation of small polaron [35].

The last possible defect we like to cover is the phosphorus vacancy, which should have relatively high energy of formation and very small concentrations. However, non-negligible deficiency of P was observed in LiFePO_4 experimentally [36]. Sumanov et al. suggested that the P deficiency in hydrothermally synthesized LiFePO_4 can be explained by partial replacement of PO_3^{4-} polyanion by four hydroxyl groups [1]. In their work, the LiFePO_4 samples were prepared from the aqueous solutions with a low concentration of initial reagents: H_3PO_4 , $\text{LiOH}\cdot\text{H}_2\text{O}$, $\text{FeSO}_4\cdot 7\text{H}_2\text{O}$, and ascorbic acid taken in the 1:3:1:1 molar ratio, in water (just to maximize the amount of the defects). Using the Powder X-ray (PXRD) and Neutron Diffraction analysis the presence of the antisite Li-Fe defects and phosphorus deficiency were determined. Additionally, the change of iron oxidation state from Fe^{2+} to Fe^{3+} was identified. Among a series of samples, for example, in the case of $\text{Li}_{0.93}\text{Fe}_{1.07}\text{P}_{0.84}\text{O}_4$, the PXRD determined composition implies that 68% of Fe should be in Fe^{3+} state for charge balance. However the Mössbauer spectroscopy shows the only 4% of Fe is in Fe^{3+} state. Such behavior indicates that some charge compensation mechanism should exists. The infrared (IR)-spectroscopy showed the presence of OH-bonds within the crystal, which allowed to assume that P deficiency is caused by OH defects. The structure of OH-defects in LiFePO_4 cannot be determined from the experiment, therefore their computational study is required. Accurate knowledge of hydrogen positions within the phosphorus vacancy as well as their formation energies can be obtained with density functional theory (DFT) computations.

1.6 OH defects in olivine ($\text{Mg}, \text{Fe}\text{SiO}_4$ minerals

LiFePO_4 share the same crystal structure with olivine mineral with typical formula $(\text{Mg}, \text{Fe})\text{SiO}_4$. This mineral is abundant in Earth mantle and was extensively studied previously. In particular, it is well established that olivine minerals contains significant amount of structural water blue (add refs). It is confirmed that hydrogen resides as a substitution defect in place of Fe or Si sites forming OH groups blue (add refs). The best investigated material in terms of OH defects is Mg_2SiO_4 , where Si or Mg atom is replaced with four or two hydrogen atoms [37]. The presence of OH defects within the structure of Mg_2SiO_4 was confirmed by IR-spectroscopy studies [38]. According to ab initio calculations [39], the formation energy of Si vacancy is lower than that of Mg vacancy in Mg_2SiO_4 . However, it was not clear for a long time whether H substitute Mg or Si in Mg_2SiO_4 . Only in the recent study it was established that both cases are possible depending on temperature and pressure [40]

In the case of LiFePO₄ the situation is even more complicated, since hydrogen can replace three species: Li, Fe, or P. Moreover, LiFePO₄ lattice contains 5 tetrahedral and 2 octahedral non-equivalent voids per formula unit, each of them can be a suitable alternative for hydrogen position.

Chapter 2

Methodology

2.1 Density Functional Theory key concepts

For many-body electronic structure calculations the Born–Oppenheimer approximation is used to consider the electrons as moving and the nuclei as stationary, the last one generate a static external potential V . A wavefunction $\Psi(\mathbf{r}_1, \dots, \mathbf{r}_n)$ is used for describing the many-electron time-independent Schrödinger equation in the stationary electronic state, eq. 2.1.

$$\hat{H}\Psi = [\hat{T} + \hat{V} + \hat{U}]\Psi = \left[\sum_i^N \left(-\frac{\hbar^2}{2m_i} \nabla_i^2 \right) + \sum_i^N V(\mathbf{r}_i) + \sum_{i < j}^N U(\mathbf{r}_i, r_j) \right] \Psi = E\Psi \quad (2.1)$$

Here N is the number of electrons in the system, \hat{H} is the Hamiltonian, E is the total energy, \hat{T} is the kinetic energy, \hat{V} is the potential energy in the external potential of positively charged nuclei, \hat{U} is the electron–electron interaction energy. The many-electron wave function $\Psi(\mathbf{r}_1, \dots, \mathbf{r}_n)$ is represented with Slater determinant and single-particle wave functions. The Hartree–Fock method can be used to solve the problem, however its application is limited to periodic systems, as the wave function depends on $3N$ variables. The Density Functional Theory (DFT) gives an opportunity to solve the problem in a different way. In this case the electron density $n(\mathbf{r})$ is a key variable with dependency just on three spatial coordinates, which is given by eq. 2.2 for a normalized Ψ .

$$n(\mathbf{r}) = N \int d^3\mathbf{r}_2 \dots \int d^3\mathbf{r}_N \Psi^*(\mathbf{r}_1, \mathbf{r}_2, \dots, \mathbf{r}_N) \Psi(\mathbf{r}_1, \mathbf{r}_2, \dots, \mathbf{r}_N) \quad (2.2)$$

Theoretical justification of density functional theory usage is confirmed by the Hohenberg–Kohn theorems for the ground states. The first theorem states that the ground state properties of a many-electron system are uniquely determined by electronic density, eq. 2.3. Thus, the complex dependency on $3N$ electronic coordinates in the Hartree–Fock method converts to 3 coordinates in electronic density functional.

$$\Psi_0 = \Psi[n_0] \quad (2.3)$$

The second theorem claims that the electron density that minimizes the energy of the overall functional is the true electron density corresponding to the full solutions of the Schrödinger equation, eq. 2.4.

$$E_0 = E[n_0] = \langle \Psi[n_0] | \hat{T} + \hat{V} + \hat{U} | \Psi[n_0] \rangle \quad (2.4)$$

Generally, the external potential \hat{V} can be rewritten via electronic density as in the equation 2.10. In comparison with universal $T[n]$ and $U[n]$ functionals, the $V[n]$ functional is dependent on the system under study. For each system the minimization of the full energy with relation to the density $n(\mathbf{r})$ is necessary 2.6.

$$V[n] = \int V(\mathbf{r}) n(\mathbf{r}) d^3\mathbf{r} \quad (2.5)$$

$$E[n] = T[n] + U[n] + \int V(\mathbf{r}) n(\mathbf{r}) d^3\mathbf{r} \quad (2.6)$$

The variational task of finding the minimum value of $E[n]$ can be solved using Kohn- Sham equations, where many-particle interactions are taken into account by the effective potential acting on non-interacting particles.

The energy functional is provided in the equation 2.7.

$$E_s[n] = \langle \Psi_s[n] | \hat{T} + \hat{V}_s | \Psi_s[n] \rangle \quad (2.7)$$

Be solving the Kohn-Sham equations for non-interacting electron system in the effective potential the φ orbitals (2.8) are obtained, according to which the electron density of the whole many-electron system is calculated (2.9).

$$[-\frac{\hbar^2}{2m} \nabla_i^2 + V_s(\mathbf{r})] \varphi_i(\mathbf{r}) = \varepsilon_i \varphi_i(\mathbf{r}) \quad (2.8)$$

$$n_s(\mathbf{r}) = \sum_i^N |\varphi_i(\mathbf{r})|^2 \quad (2.9)$$

Once the electronic density is known the effective potential is calculated according to the following equation:

$$V_s(\mathbf{r}) = V(\mathbf{r}) + \int \frac{e^2 n_s(\mathbf{r}')}{|\mathbf{r} - \mathbf{r}'|} d^3\mathbf{r}' + V_{XC}[n_s(\mathbf{r})] \quad (2.10)$$

where $V_{XC}[n_s(\mathbf{r})]$ is exchange-correlation functional which effectively takes into account many-particle interactions. However, the exact form of this potential is not known and should be ap-

proximated. The examples of such approximations are Local Density Approximation (LDA) and Generalized Gradient Approximations (GGA).

In practice, one start from a guess electronic density and proceed with iterative solution of the provided equations until self-consistency is achieved.

2.2 Computational details

The atomic structure and energetics of intrinsic OH defects in $\text{Li}(\text{Fe},\text{Mn})\text{PO}_4$ was investigated by first-principles calculations. All calculations were based on the Density Functional Theory (DFT) using a generalized-gradient approximation (GGA) [41], Perdew–Burke–Ernzerhof (PBE) exchange-correlation model and Projector-Augmented-Wave (PAW) method as implemented in the VASP program [42]. A python-based framework (SIMAN) [43] was used for the preparation and analysis of DFT calculations.

The investigation of pure and defective $\text{Li}(\text{Fe},\text{Mn})\text{PO}_4$ was performed using one unit cell, which contains four formula units. The energy cut-off was equal to 400 eV, the k-point mesh is $3 \times 4 \times 5$ for one unit cell. The Gaussian smearing was used for Brillouin-zone integration. All calculations were spin-polarized with ferromagnetic state of $\text{Li}(\text{Fe},\text{Mn})\text{PO}_4$. The DFT+U calculations were carried out using Dudarev scheme. The value of U for Fe is 4 eV [44].

The optimization of lattice constants was performed by a volume scan method using seven fixed volumes ($\pm 5\%$). The relaxations of atomic positions and cell shape were performed using quasi-Newton algorithm implemented in the VASP code. The relaxation of atomic positions was performed until the maximum force acting on atoms was less than $0.05 \text{ eV}/\text{\AA}$.

All calculations are performed using supercomputer clusters (Skoltech clusters Magnus and Pardus, DTU cluster Niflheim). The visualization of atomic structures was performed in Jmol and Vesta programs.

2.3 Scan of hydrogen potential energy surface

To study the structure of $\text{PO}_4/(\text{OH})_4$ defects in detail we performed a full scan of the potential energy surface (PES) for hydrogen atoms inside and around the phosphorus vacancy.

The PES was constructed iteratively using single-point calculations for each added hydrogen atom. As a result a separate PES construction was obtained for each considered defect composition: PO_4/HO_4 , $\text{PO}_4/\text{H}_2\text{O}_4$, $\text{PO}_4/\text{H}_3\text{O}_4$, and $\text{PO}_4/\text{H}_4\text{O}_4$. The first PES ($\text{PO}_4/\text{H}_1\text{O}_4$) gives the minimum energy position of one H in the P vacancy. This configuration, after full atomic optimization was fixed and used for constructing the second PES ($\text{PO}_4/\text{H}_2\text{O}_4$ defect). In the same manner the third PES ($\text{PO}_4/\text{H}_3\text{O}_4$) was constructed from the optimized lowest energy $\text{PO}_4/\text{H}_2\text{O}_4$ configuration

and the fourth PES ($\text{PO}_4/\text{H}_4\text{O}_4$) - from the optimized lowest energy $\text{PO}_4/\text{H}_3\text{O}_4$ configuration.

Since it is known that H should form covalent bond with O, only spherically symmetrical PES were considered around each of the four oxygens left after P removal. The example of PES is provided in Figure 3.12. The energy of H used for PES construction was calculated according to the equation:

$$E_{\text{H}} = \frac{1}{n} [E(\text{LiFeP}_{1-x}\text{H}_{nx}\text{O}_4) - E(\text{LiFeP}_{1-x}\text{H}_{(n-1)x}\text{O}_4) - \frac{1}{2}xE(\text{H}_2)] \quad (2.11)$$

where $E(\text{LiFeP}_{1-x}\text{H}_{nx}\text{O}_4)$ and $E(\text{LiFeP}_{1-x}\text{H}_{(n-1)x}\text{O}_4)$ are the total energies of unit cells n and $n-1$ H atoms, respectively, and $E(\text{H}_2)$ is a total energy of H_2 molecule in a gas phase. The E_{H} is visualized by assigning a particular color within red-green-blue spectrum, from blue (for lower energy) to red (as high energy).

The programming code for PES scan and its visualization is presented in Appendix A, section A.1–A.5.

2.4 Molecular Dynamics study

The investigation of $\text{Li}(\text{Fe,Mn})\text{P}_{1-x}\text{H}_{4x}\text{O}_4$ dynamics at elevated temperatures was performed for $1\times2\times2$ supercell with 115 atoms using molecular dynamics (MD) simulation as implemented in the VASP code. The initial atomic configuration of PO_4/HO_4 defect was used from the PES study. For MD study the precision of calculations was reduced. The k-point spacing was set to 0.7 \AA^{-1} and 300 eV energy cut-off was used. MD simulations were performed at several fixed temperatures: 690 K, 890 K and 1390 K. These values correspond to the annealing temperatures during synthesis. A time step of 1 fs was used for the integration of motion equations, and 2000 or 10000 ionic steps were used, which corresponds to 2 ps and 10 ps simulation time runs.

Chapter 3

Results

3.1 Calculation of bulk properties

The current work is aimed to study the structure of OH defects in LiFePO₄ and LiMnPO₄. However, first of all the calculation of the lattice constants and electric properties of pure material are necessary to benchmark the chosen calculation parameters. The LiFePO₄ unit cell obtained after optimization of lattice constants and atomic positions is shown in Figure 3.1. The obtained lattice constants for LiFePO₄ and LiMnPO₄ are in good agreement with literature data, which is seen from Table 3.1.

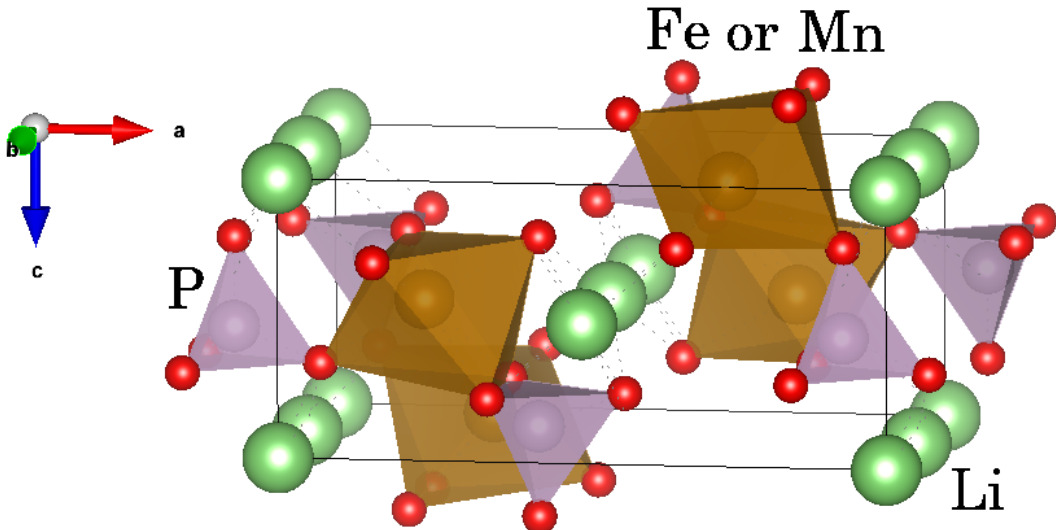


Figure 3.1: Schematic unit cell and features of LiFePO₄ and LiMnPO₄

The calculated total density of states (DOS) is shown in Figure 3.2 for LiFePO₄ and LiMnPO₄ compounds. In the case of LiMnPO₄ the obtained band gap is 2.1 eV, which agrees with insulating behaviour of this material, observed in experiment. However, the value of band gap is underestimated, which is a well known problem of GGA calculations for transition metal compounds, where localization of d-electrons results in band gap opening. In the case of LiFePO₄ our GGA calculations predict the absence of band gap. By using Hubbard correction, the localization of d-electrons is taken into account and the band gap can be reproduced in agreement to the experiment. While

Table 3.1: Lattice constants and band gaps for LiFePO_4 and LiMnPO_4 in comparison to literature data

Space group	LiFePO_4		LiMnPO_4	
	Current work	Ref.	Current work	Ref.
$a, \text{\AA}$	10.33	10.32 [19]	10.56	10.45 [19]
$b, \text{\AA}$	6.01	6.01 [19]	6.15	6.10 [19]
$c, \text{\AA}$	4.73	4.69 [19]	4.79	4.74 [19]
Band gap, eV	0.0 (GGA) 3.7 (+U) [26]	0.2 (GGA)	2.1 (GGA)	2.0 (GGA) 3.8 (+U) [26]
Voltage, V	3.4 [45]		4.1 [45]	
Capacity, mAh/g	150 [45]		140 [45]	

the Hubbard correction has significant influence on formation energies, the GGA without U can still be used for describing structural features of point defects as will be shown further.

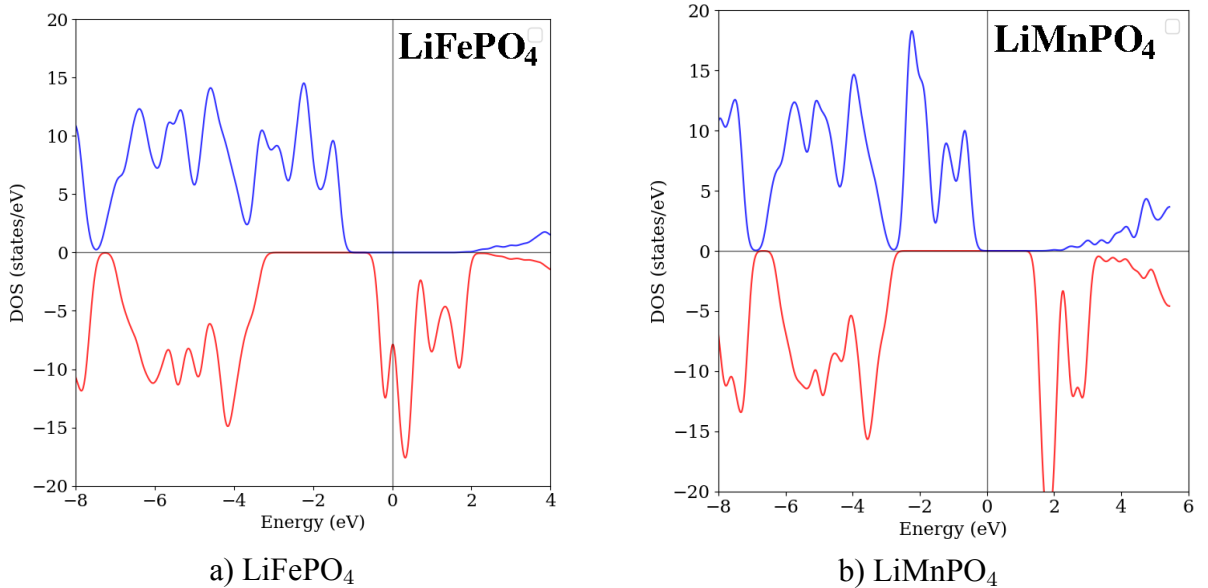


Figure 3.2: Calculated total density of states with GGA approach for LiFePO_4 and LiMnPO_4 compounds.

3.2 Structure and energetics of H interstitial and Li/H and Fe/2H substitution defects

In this section the formation energy of P vacancy and several OH defects are calculated with GGA and GGA+U methods. To compare interstitial H and substitutional Li/H and Fe/2H we use a simple thermodynamic model which takes into account the stability region LiFePO_4 phase.

Though this model does not correspond directly to the synthesis conditions, which are too complicated for theoretical reproductions, it gives reasonable estimation of defect formation energies and allows to compare them with each other. We begin from Li-Fe-P-O phase diagram, which was constructed from first-principles by Ong et al. [46]. The region of interest is formed by Li_3PO_4 , LiFePO_4 and Fe_2O_3 end phases (Figure 3.3). The chemical potential, $\mu(X)$ of each species is then defined using end phases and the chemical potential of O_2 . The latter is determined from the experiment conditions and changed from the temperature, pressure, and concentration of reductive chemical additions. According to Ong et al. the relevant values of oxygen chemical potential varies from -13.10 to -11.52 eV [46]. The chemical potential of hydrogen is calculated with respect to water molecule in the gas phase according to the following equation (3.1):

$$\mu(\text{H}) = \frac{1}{2}[\mu(\text{H}_2\text{O}_{\text{gas}}) - \frac{1}{2}\mu(\text{O}_2)] \quad (3.1)$$

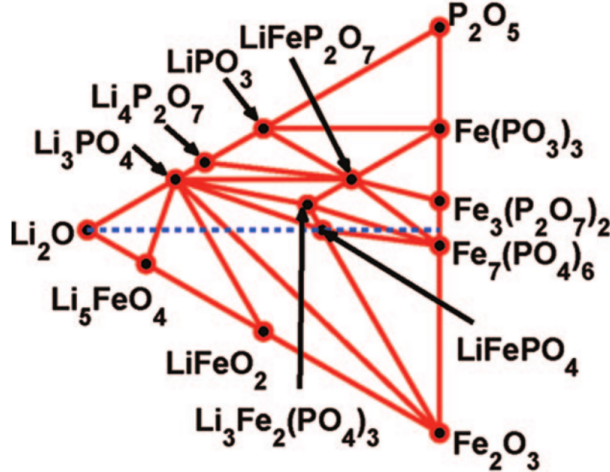


Figure 3.3: Phase diagram for LiFePO_4 compounds [46]

The energy of H_2O in the gas phase is calculated from the first-principle study at 0 (K). The chemical potentials of Li, Fe, and P species are determined from the total energies of Li_3PO_4 , LiFePO_4 and Fe_2O_3 phases according to the following equations:

$$\begin{aligned} \mu(\text{Fe}) &= \frac{1}{2}[\mu(\text{Fe}_2\text{O}_3) - \frac{3}{2}\mu(\text{O}_2)] \\ \mu(\text{Li}) &= \frac{1}{2}[\mu(\text{Li}_3\text{PO}_4) - \mu(\text{LiFePO}_4) + \mu(\text{Fe})] \\ \mu(\text{P}) &= \frac{1}{2}[3\mu(\text{LiFePO}_4) - \mu(\text{Li}_3\text{PO}_4) - 3 \cdot \mu(\text{Fe}) - 4 \cdot \mu(\text{O}_2)] \end{aligned} \quad (3.2)$$

At most oxidizing chemical potential of oxygen $\mu(\text{O}_2) = -11.52$ eV, the chemical potentials of each species are -4.650 eV for H, -5.821 eV for Li, -10.095 eV for Fe, and -10.048 eV for P.

According to the chemical potential values of each species the formation energies of Li, Fe

or P vacancies in LiFePO_4 are calculated using the energies of $\text{Li}_{1-x}\text{Vac}_x\text{FePO}_4$, $\text{LiFe}_{1-x}\text{Vac}_x\text{PO}_4$ and $\text{LiFeP}_{1-x}\text{Vac}_x\text{O}_4$ supercells, according to these equations:

$$\begin{aligned} E(\text{Li}_{\text{vacancy}}) &= E(\text{Li}_{1-x}\text{Vac}_x\text{FePO}_4) - E(\text{LiFePO}_4) + \mu(\text{Li}) \\ E(\text{Fe}_{\text{vacancy}}) &= E(\text{LiFe}_{1-x}\text{Vac}_x\text{PO}_4) - E(\text{LiFePO}_4) + \mu(\text{Fe}) \\ E(\text{P}_{\text{vacancy}}) &= E(\text{LiFeP}_{1-x}\text{Vac}_x\text{O}_4) - E(\text{LiFePO}_4) + \mu(\text{P}) \end{aligned} \quad (3.3)$$

The calculated formation energies are presented in Table 3.2.

Table 3.2: Chemical potentials of species and formation energies of vacancies in LiFePO_4 ($\mu(\text{O}_2) = -11.52$ eV) calculated with GGA and GGA+U methods

Type of atom	$\mu(X), \text{eV}$ (GGA)	$\mu(X), \text{eV}$ (GGA+U)	$E_{\text{vacancy}}, \text{eV}$ (GGA)	$E_{\text{vacancy}}, \text{eV}$ (GGA+U)
H	-4.650	-4.650	-	-
Li	-5.821	-5.239	-1.75	0.64
Fe	-10.095	-8.328	-2.48	1.40
P	-10.048	-11.626	0.38	3.46

A comparison of chemical potentials obtained with GGA and GGA+U calculations shows the difference for the iron atom, which is expected, since the U correction is applied on its d orbitals. As a result such behaviour have significant impact on formation energies of vacancies. As it can be seen from Table 3.2, the GGA without U considerably underestimates vacancy formation energies. This correlates well with the known underestimation of Li intercalation potentials and Li vacancy formation energies by GGA method in transition metal compounds. Thus, the GGA+U calculation is more appropriate for a realistic estimate of energies, but, at the same time, the atomic structure can be reproduced with GGA.

Interstitial hydrogen in octahedral voids of ideal LiFePO_4

We found two stable hydrogen positions in octahedral void of LiFePO_4 structure.

In the first case the H atom was initially placed near the Fe atom with Fe-H distance of 1.95 Å. After atomic optimization the Fe-H distance is 1.99 Å, the shortest O-H distance is 1.04 Å, and second shortest O-H distance is 1.55 Å. The H atom is located at line between O1 and O2 atoms, creating the hydrogen bond, Figure 3.4. The formation energy of such defect is equal to 3.35 eV.

In the second case the hydrogen atom was placed near the P atom (Figure 3.5 a)). After atomic relaxation the distance between the H atom and O is 1.01 Å and the distance between the hydrogen atom and the second neighboring oxygen H-O₂ is 1.84 Å, Figure 3.5. The formation energy of such defect is slightly lower and is equal to 3.22 eV.

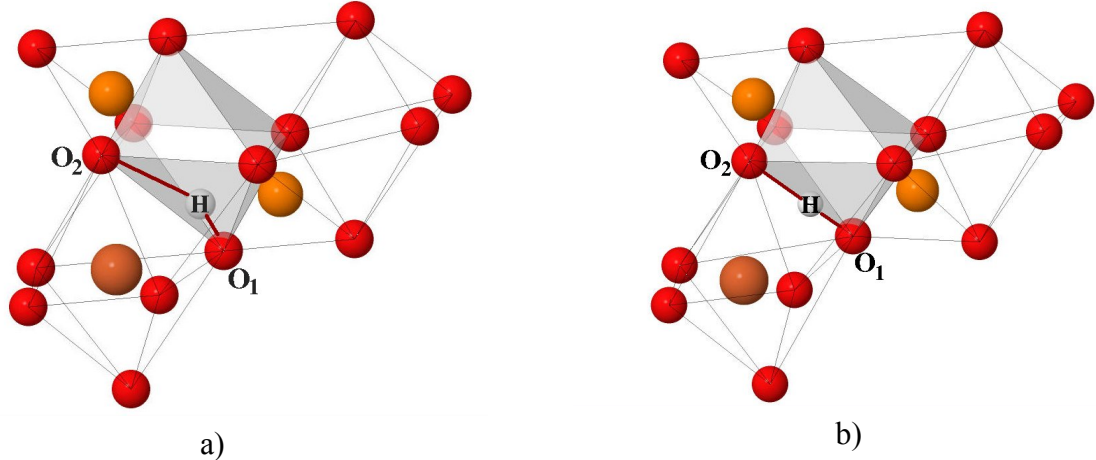


Figure 3.4: Position of H atom in octahedral void before (a) and after (b) structural optimization (case 1)

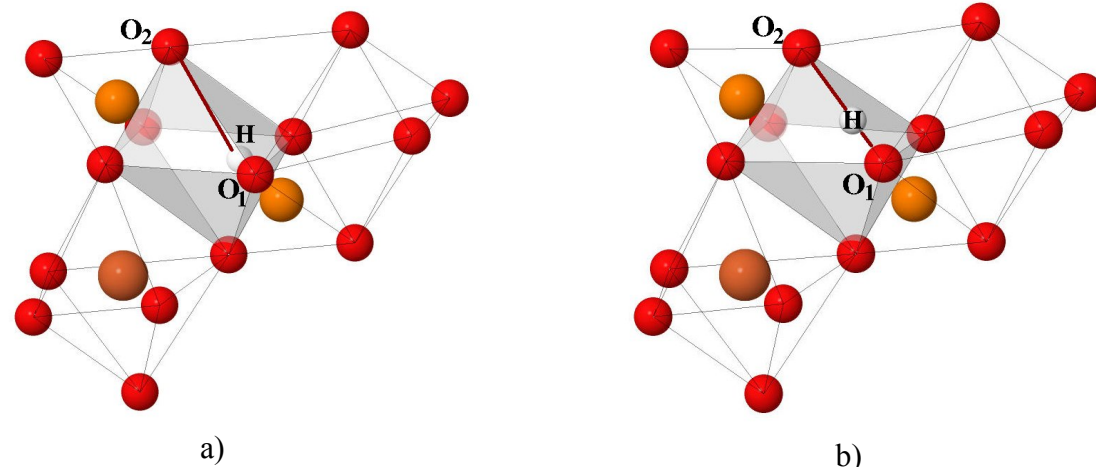


Figure 3.5: Position of H atom in octahedral void before (a) and after (b) structural optimization (case 2)

Interstitial hydrogen in tetrahedral voids of ideal LiFePO₄

Two stable hydrogen positions in tetrahedral void of LiFePO₄ structure were discovered. In the first case the H atom was placed in the center of tetrahedral void (Figure 3.6 a)). After relaxation, the distances between the interstitial H atom and other atoms changed for H-O1 from 1.84 Å to 2.54 Å, for H-O2 from 1.69 Å to 1.54 Å, and for H-Fe from 2.09 Å to 1.48 Å (Figure 3.6). It is important to note the change of distance between O2 atom and neighboring iron increases from 2.21 Å to 2.98 Å. The formation energy of such defect is equal to 3.05 eV.

In the second case interstitial hydrogen was placed near the iron with the H-O₁ distance

equal to 1.2 Å, which have changed to 0.99 Å after relaxation of the atomic positions (Figure 3.7). The formation energy of such defect is equal to 3.15 eV.

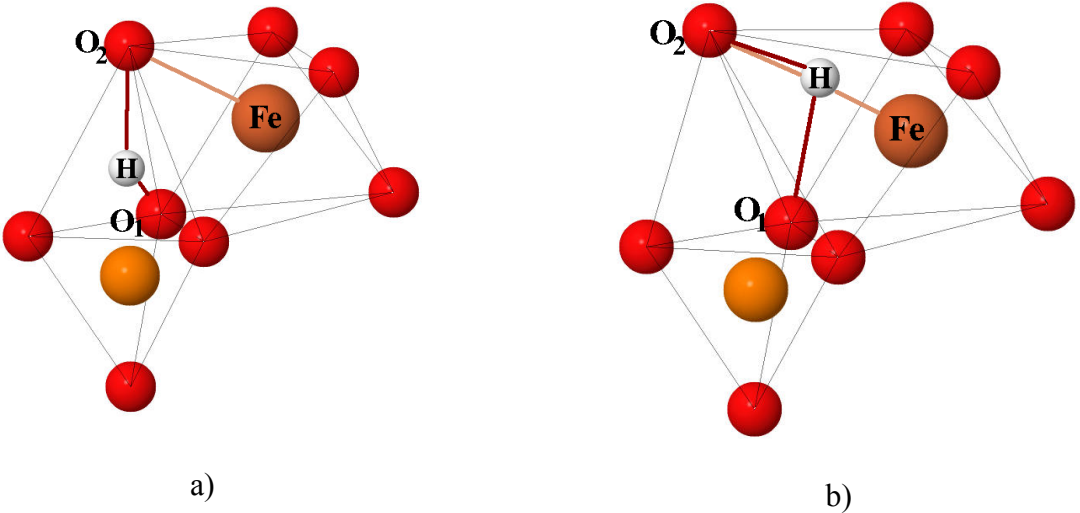


Figure 3.6: Position of H atom in tetrahedral void before (a) and after (b) structural optimization (case 1)

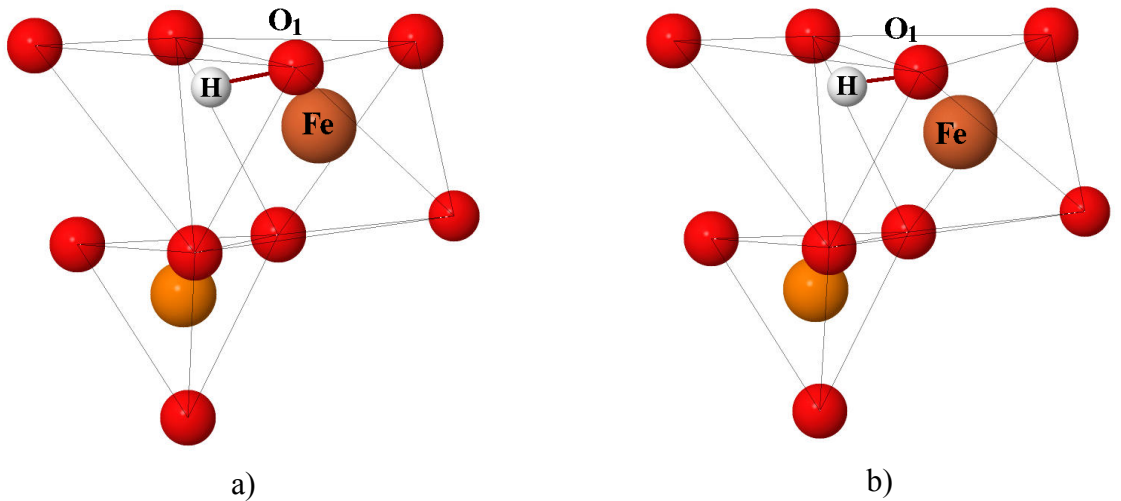


Figure 3.7: Position of H atom in tetrahedral void before (a) and after (b) structural optimization (case 2)

Substitution of lithium by hydrogen in LiFePO_4

The substitution of lithium by hydrogen was considered. In this case the change of the hydrogen position and the relative distances are shown in Figure 3.8. After the atomic relaxation the distance between the hydrogen atom and neighboring oxygen atom $H-O_1$ has been changing from 0.99 Å to 1.00 Å, Figure 3.8. The formation energy of Li/1H substitution defect was calculated according to equation (3.4). The corresponding formation energy of such substitution defect was equal to 0.18 eV for oxygen chemical potential $\mu(O_2) = -11.52$ eV and 0.38 eV for $\mu(O_2) = -13.1$ eV, Table 3.3.

$$\mu(\text{Li}_{\text{vacancy}}) = E(\text{Li}_{1-x}\text{Vac}_x\text{FePO}_4) - E(\text{LiFePO}_4) + \mu(\text{Li}) - \mu(\text{H}) \quad (3.4)$$

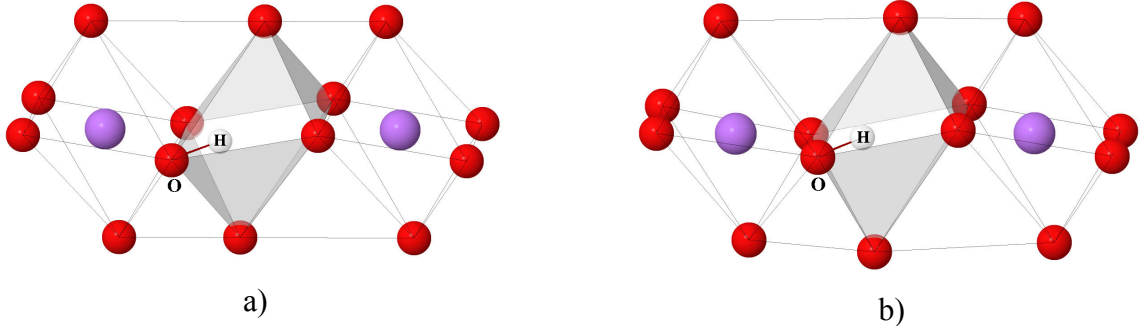


Figure 3.8: Changes of substitution of lithium by hydrogen structural optimization

Substitution of iron by hydrogen in LiFePO₄

The next considered substitution defect is hydrogen in place of iron atom. According to the oxidation state of iron in LiFePO_4 , two H should replace one Fe to achieve initial charge balance. The distinction in the distance between neighboring atoms is presented in Figure 3.9. In this case the distances between first hydrogen and oxygen atoms H_1-O_1 were changed from 1.25 Å to 1.00 Å; H_1-O_3 – from 2.71 Å to 2.00 Å. The distances between second hydrogen and neighboring oxygen atoms were changed for H_2-O_2 from 1.20 Å to 0.99 Å, for H_2-O_3 from 2.27 Å to 1.94 Å. The formation energy of this defect is calculated according to the equation (3.5) and is equal to 0.30 eV for oxygen chemical potential $\mu(\text{O}_2) = -11.52$ eV and 0.50 eV for $\mu(\text{O}_2) = -13.1$ eV, Table 3.3.

$$E(\text{Fe}_{\text{vacancy}}) = \frac{1}{2}(E(\text{LiFe}_{1-x}\text{Vac}_x\text{PO}_4) - E(\text{LiFePO}_4) + \mu(\text{Fe}) - 2\mu(\text{H})) \quad (3.5)$$

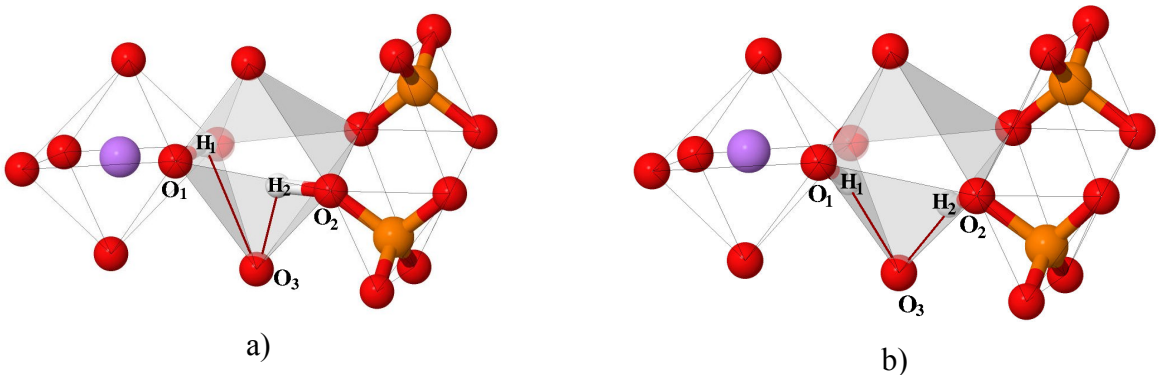


Figure 3.9: Changes of substitution of iron by two hydrogen after structural optimization

According to the data from Table 3.3, the value of each substitution defect formation energy notably depends on the calculation method: GGA without Hubbard correction gives lower forma-

Table 3.3: Calculated formation energies of interstitial and substitution OH defects in LiFePO₄

Interstitial defect	E_{form} , eV (GGA) $\mu(O_2)=-11.52$ eV	E_{form} , eV (GGA) $\mu(O_2)=-13.1$ eV	E_{form} , eV (GGA+U) $\mu(O_2)=-13.1$ eV
Oct1	3.35	2.96	—
Oct2	3.22	2.83	—
Tet1	3.05	2.66	—
Tet2	3.15	2.76	—
Li/1H	0.18	0.38	0.89
Fe/2H	0.30	0.50	0.88

tion energy in comparison with GGA+U method, where the localization of d-electrons is taken into account.

Thus, the GGA+U approach is crucial for calculating the substitution defect formation energy. At the same time, GGA without U correction is appropriate for describing structural features of point defects.

3.3 Potential energy surface of four H atoms in P vacancy

In the case of previously considered point defects the lowest energy configurations could have been determined by local optimization algorithms. However, in the case of P replacement by four H, numerous metastable configurations require to perform a search for global minimum. To achieve this we employ a scan of potential energy surface (PES) of H inside and near the P vacancy. The algorithm of PES construction is described in Methods section.

The P tetrahedra in LiFePO₄ structure is highlighted in Figure 3.10. This figure shows the pseudo layered structure of LiFePO₄ normal to the c-axes and two planes Plane₁ and Plane₂ used further for visualization. As it was explained in Methods section the considered PES has spherical shape around oxygen atoms. To simplify its visualization we will show only those atoms and points that correspond to the slice with ~ 2 Å thickness above Plane₁ (Plane 1a), below Plane₁ (Plane 1b) and below Plane₁ (Plane 2). The corresponding slices are shown in Figure 3.11.

As a first step the P vacancy was created by removing the P atom followed by atomic optimization. Then the PES for H was considered around each of the four O using spherically symmetrical grid of points generated by especially developed python code, provided in Appendix A, section A.1–A.5. The total energy of H at each point was obtained from single point calculations

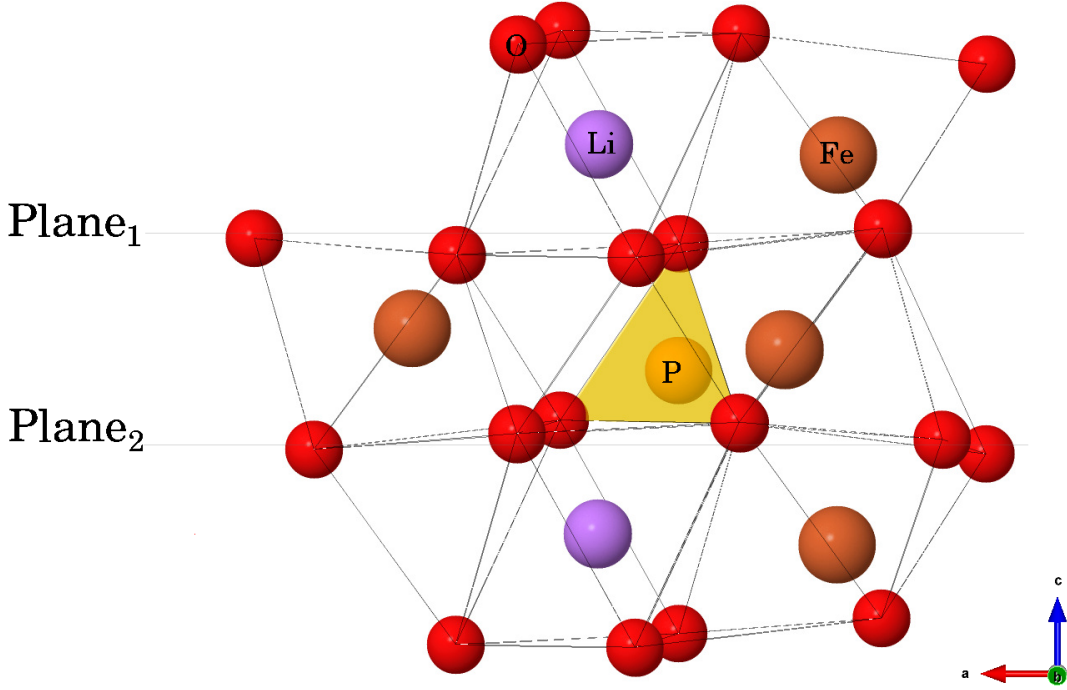


Figure 3.10: LiFePO_4 with highlighted P tetrahedron. The adjacent polyhedral voids can be seen.

without atomic relaxation. As will be shown further such approach is reasonable to identify the lowest energy configurations.

Around each of the four oxygen atoms several filled and empty voids are located. In addition to Li and Fe octahedrons each oxygen is surrounded by eight tetrahedral voids (in pictures below they will be marked using gray colored numbers) and six octahedral voids (marked using black colored numbers). The P vacancy tetrahedron is highlighted using green color.

3.3.1 PES for $\text{PO}_4/\text{O}_4\text{H}_1$ defect

Our first step of $\text{PO}_4/(\text{OH})_4$ defect investigation is the study of the substitution phosphorus by one hydrogen atom $\text{PO}_4/\text{O}_4\text{H}_1$. We considered 153 positions of H atom around oxygen O₁ (reduced coordinates: -0.046, 0.125, 0.147) changing O-H distance between 0.9 Å and 1.3 Å. For each structure the single point static calculation of energy was performed. The energy of each hydrogen atom in its position was calculated according to (2.11) equation. The obtained slices of PES, where different energies are shown with color are provided in Figure 3.12. The dark blue colors show the lowest energy positions of H atom and dark red colors show high energy positions. It is unfavourable for H to be near iron or lithium atoms, while it prefers to be in the tetrahedral void left after P removal (3tet) and in the octahedral void (4oct).

We took several lowest energy H positions in the different voids and performed atomic relaxation. After relaxation the H atom has moved either to 3tet or 4oct voids with the latter being

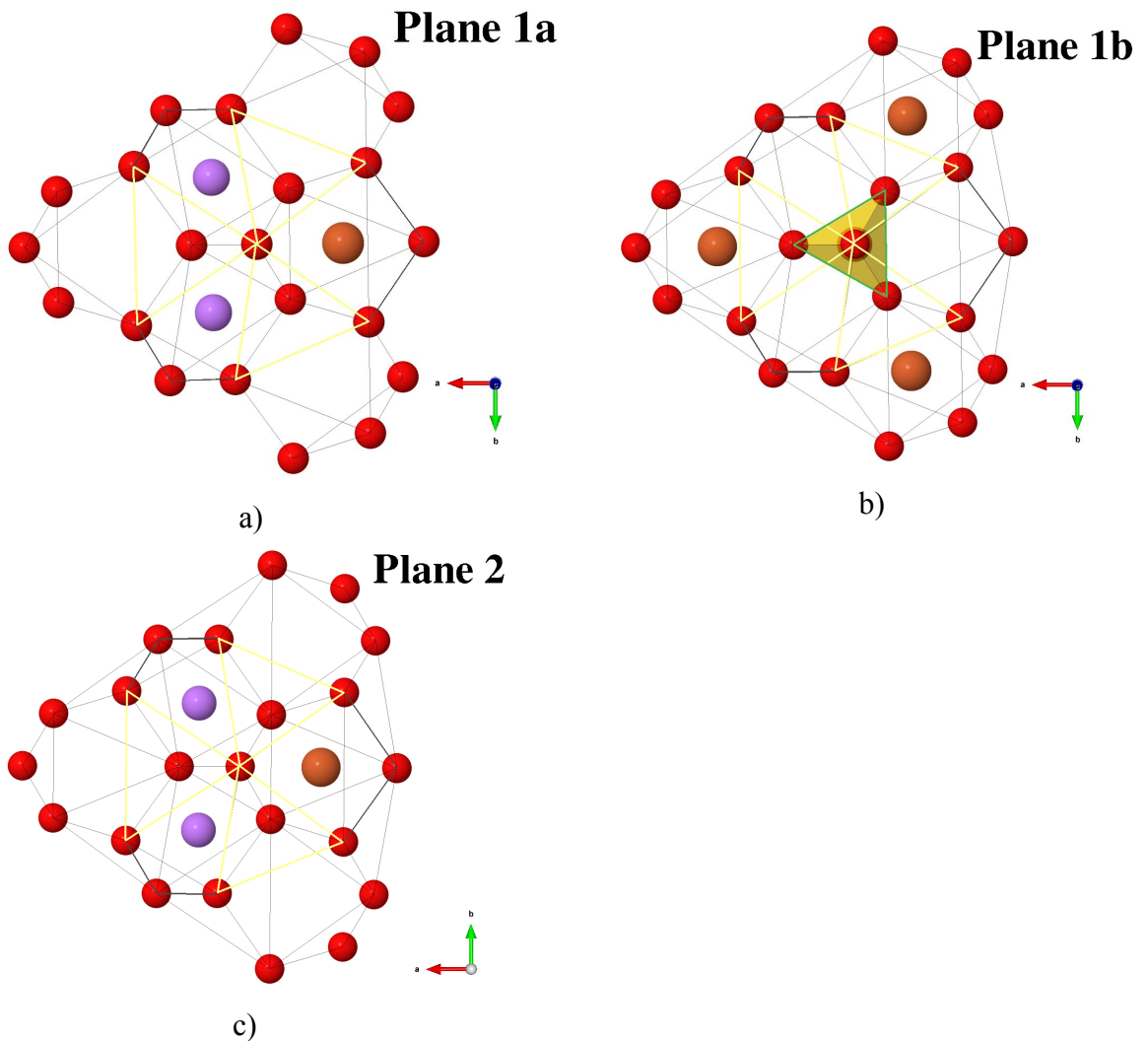


Figure 3.11: a) The considered slices of LFP structure used for visualization of PES.

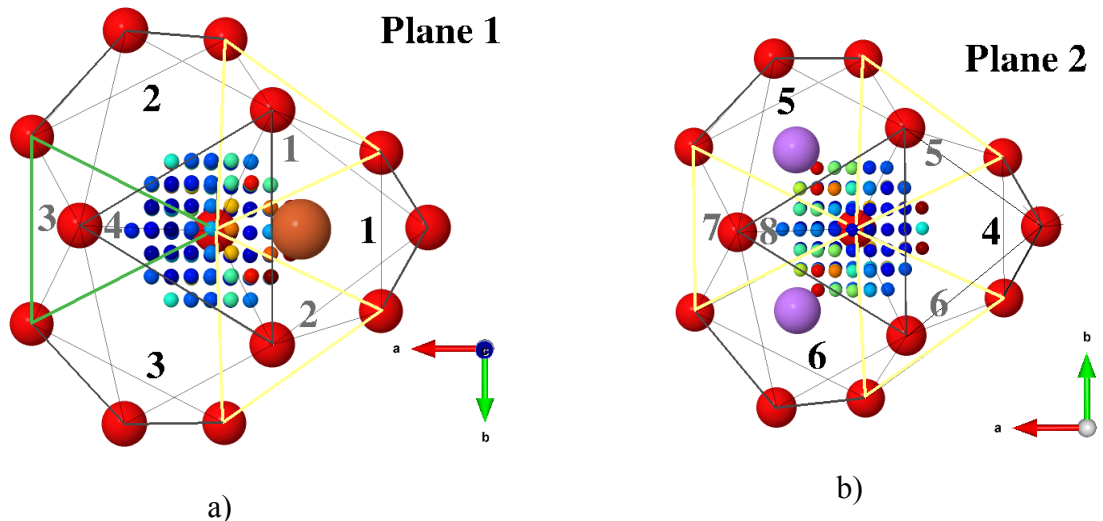


Figure 3.12: Two slices of H potential energy surface for $\text{PO}_4/(\text{OH})_1$ defect. The low and high energies of H are shown with rainbow colors from dark blue to dark red.

higher in energy by 0.4 eV. The relative energies of final configurations obtained from different initial conditions are collected in Table 3.4.

Table 3.4: Relative energy of hydrogen after atomic optimization of several lowest energy points of PES for $\text{PO}_4/(\text{OH})_4$ defect. The second and fourth columns show initial and final voids for H.

No	Initial → final	$\Delta E, \text{eV}$	No	Initial → final	$\Delta E, \text{eV}$
a	4tet → 3tet	0.000	g	5tet → 4oct	0.416
b	7tet → 3tet	0.001	h	8tet → 4oct	0.419
c	3tet → 3tet	0.002	k	4oct → 4oct	0.420
d	3oct → 3tet	0.002	l	2tet → 4oct	0.432
e	2oct → 3tet	0.003	m	1tet → 4oct	0.483
f	6tet → 4oct	0.415			

In fact, the lowest energy position of H is located on the edge between tetrahedral voids 4 and 3, which is shown in Figure 3.13. Here, it should be noted that PES constructed with single point calculations gives quite reasonable estimation of the most favourable hydrogen position.

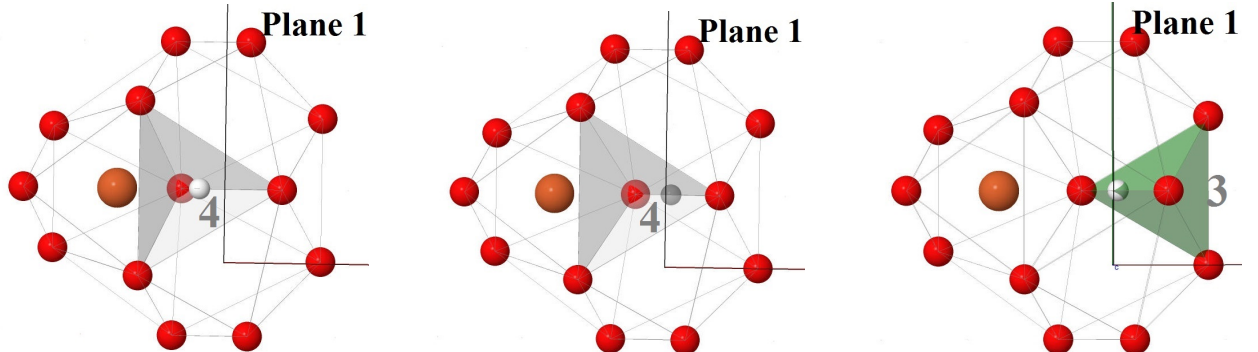


Figure 3.13: Relaxation of H from tetrahedral void 4 to tetrahedral void 3. Left figure: before relaxation; Center and right figures: after relaxation.

In the same manner the relaxation of H is observed for octahedral voids (number 2 and 3 black) and tetrahedral voids (number 3 and 7 grey). The H movement from tetrahedral site (number 7 grey) to the tetrahedron with P vacancy (number 3 grey) is shown in Figures 3.14 and 3.15 using different slices. These hydrogen atom positions have higher energy than in the case of 3tet. Hydrogen atoms from other positions: the octahedral void (num.4 black) and tetrahedral sites with (num.1, 2, 5, 6, and 8 grey) have even higher energy. In these cases atoms from their initial positions move to the boundary with octahedral void (num.4 black), Table 3.4.

According to calculated results, some outcomes can be concluded:

1. Potential energy surface scan of hydrogen grid distribution shows the appropriate and

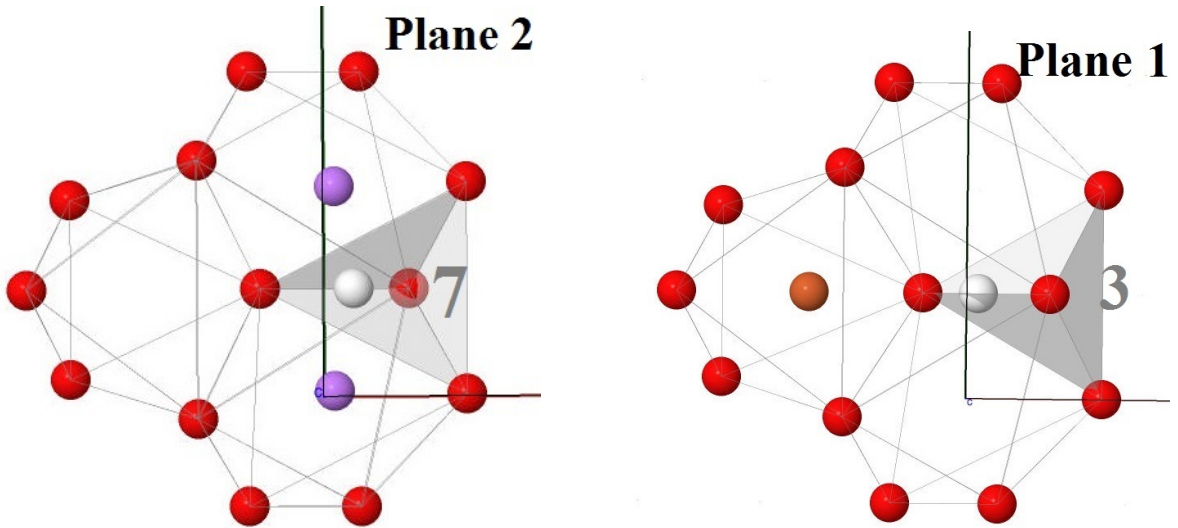


Figure 3.14: Movement of hydrogen atom from 7 tetrahedral void to 3 tetrahedral void. Pictures on the left side – before relaxation; pictures in the right side – after relaxation.

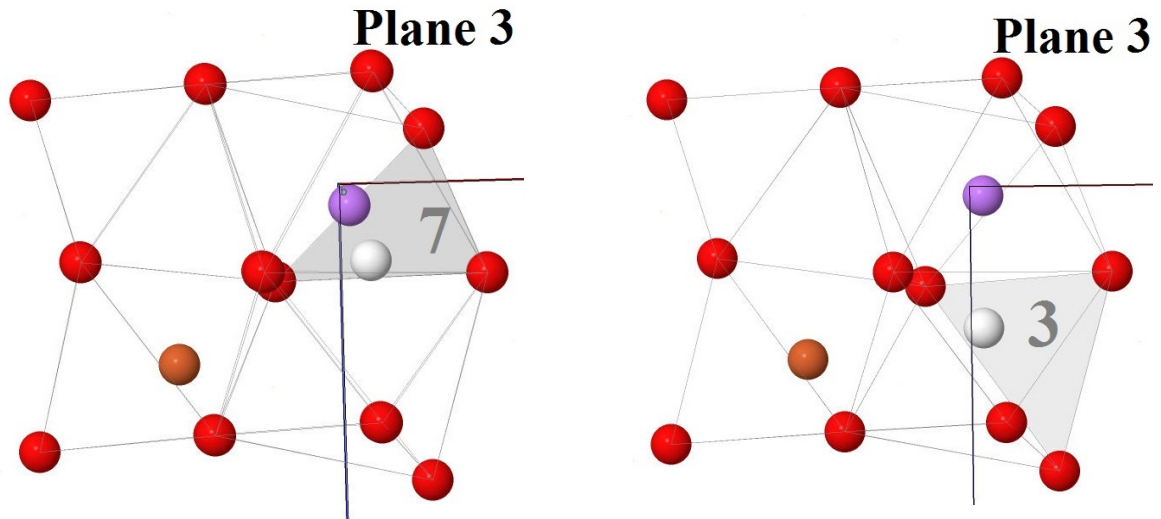


Figure 3.15: Movement of hydrogen atom from 7 tetrahedral void to 3 tetrahedral void – one of more stable position: pictures on the left side – before relaxation; pictures in the right side – after relaxation in the plane 3

inappropriate positions of hydrogen in the phosphorus deficient LiFePO₄ material. 2. PES scan is a useful tool for prediction of possible equilibrium hydrogen positions; 2. According to further calculation of atomic positions relaxation the equilibrium sites of hydrogen atom in phosphorus vacancy tetrahedron were confirmed; 3. The movement of hydrogen atom between tetrahedral sites (num.4 and 3 grey) was established as a more appropriate due to its low formation energy.

3.3.2 PES for PO₄/O₄H₂ defect

As a next step we constructed a PES for hydrogen around second oxygen of the phosphorus-defective tetrahedron, while the first hydrogen was fixed in its equilibrium position (from the first

study of $\text{PO}_4/(\text{OH})_1$). The obtained PES slices are shown in Figure 3.16.

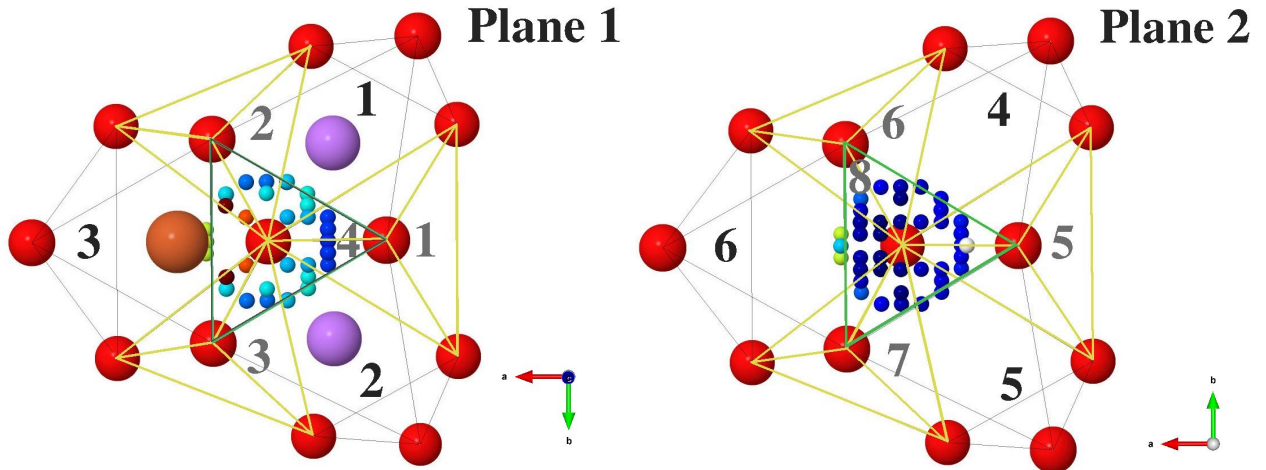


Figure 3.16: Hydrogen distribution around second oxygen in phosphorus-defective tetrahedral site (8 grey number)

The hydrogen atoms inside the phosphorus vacancy tetrahedral site (num.8 grey in Plane 2) have lower energy in comparison to other outside hydrogen atoms (for example, near iron atom in the Plane 1 figure). The atomic positions relaxation was provided for each LiFePO_4 system with two hydrogen atoms: near first oxygen in its equilibrium position and second oxygen in various position. The formation energy of each site of the second hydrogen was calculated and the Table 3.5 was completed.

Table 3.5: Energy of hydrogen in different polyhedral sites around second oxygen

No	Initial → final	$\Delta E, \text{eV}$	No	Initial → final	$\Delta E, \text{eV}$
a	5oct → 7tet	0.0000	h	3tet → 6tet	0.0011
b	4oct → 6tet	0.0003	k	2tet → 7tet	0.0012
c	1oct → 7tet	0.0003	l	6oct → 6tet/8tet	0.0022
d	8tet → 6tet/8tet	0.0007	m	4tet → 1tet	0.7166
e	2oct → 6tet	0.0007	n	5tet → 1tet	0.7185
f	7tet → 7tet	0.0008	o	1tet → 1tet	0.7185
g	6tet → 6tet/8tet	0.0011			

The movement of two hydrogen atoms from initial positions to final advantageous positions after the atomic relaxation calculation is presented in the Figure 3.17.

According to this information, some outcomes can be concluded:

1. The hydrogen atom moves from the octahedral void (num.5 black) to the tetrahedral void (num.7 grey) and has the lowest formation energy in comparison to other hydrogen positions;
2. The similar low-energy state can be observed for hydrogen atoms in the octahedral voids (num.1, 2, 4 black) and in the tetrahedral voids num.2, 3, 6, 7, 8 grey), which have moved to the edge of the tetrahedral voids (num.6, 7 and 8 grey) during the relaxation of atomic structure;
3. The energetically-advantageous position can be also observed in the tetrahedral void (num.4 grey), where the hydrogen atoms from the tetrahedral voids (num.1, 4, and 5 grey) have been moved to more stable positions.

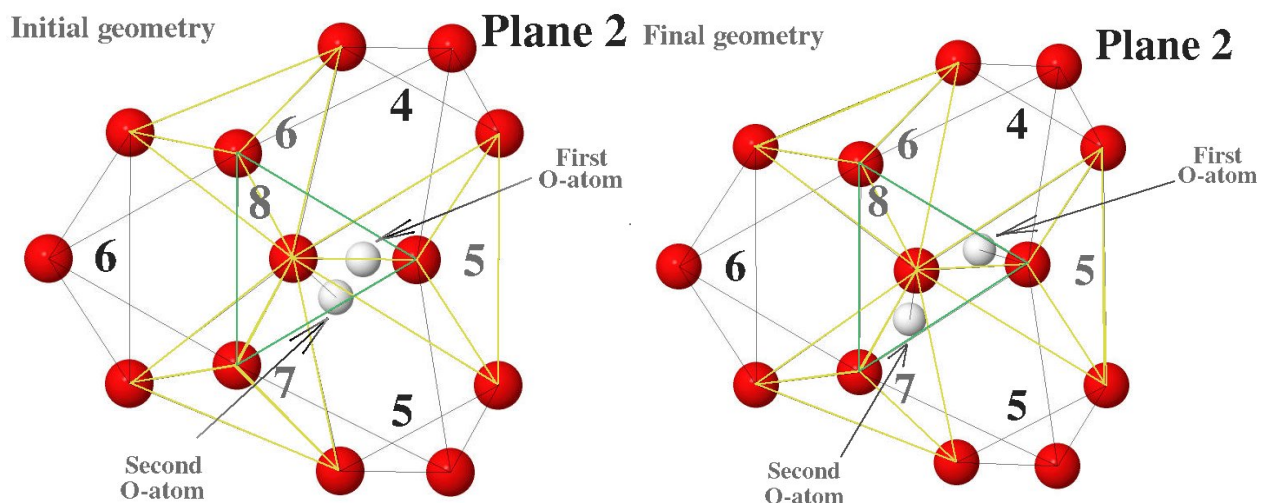


Figure 3.17: The most stable positions of two H atoms in the P vacancy before and after relaxation (grey number 8).

3.3.3 PES for $\text{PO}_4/\text{O}_4\text{H}_3$ defect

The study of hydrogen atoms distribution around the third oxygen atom in phosphorus-defective LiFePO_4 structure with the presence of two hydrogen near the first and second oxygen (from 1 and 2 steps of investigation) is described in the current paragraph.

The constructed PES is presented in Figure 3.18. According to PES, the assumption about an advantageous position of the third hydrogen atom near tetrahedral site (num.2 grey) and the octahedral site (num.5 black) can be made.

The stable positions and resulting relative energies are collected in Table 3.6.

Several conclusions can be formulated from Table 3.6:

1. Structure with lower energy is formed with the third atom, which is moved from the octahedral void (num.2 black) to the edge between the tetrahedral void (num.2 grey) and the octahedral void (num.3 black).

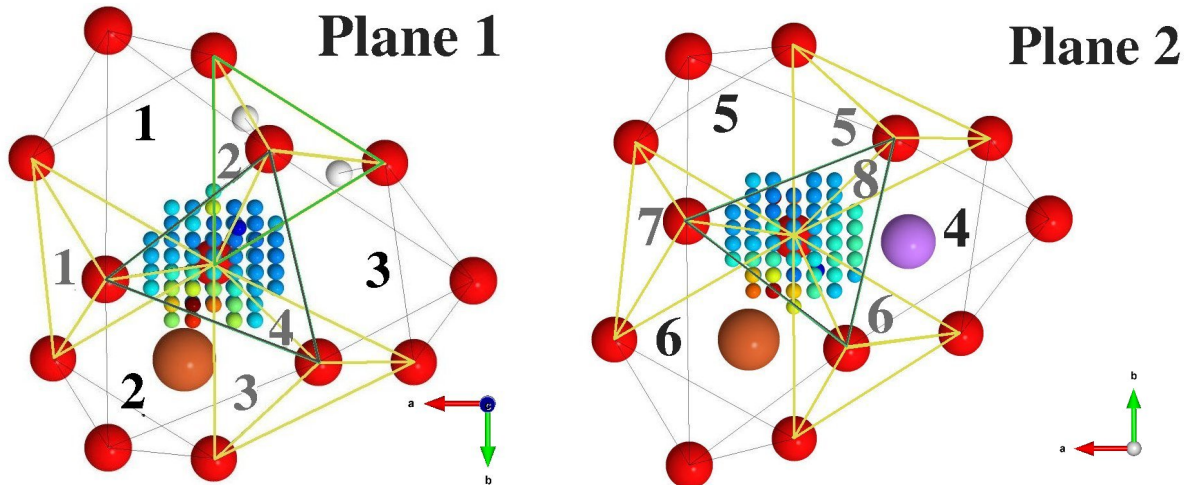


Figure 3.18: Hydrogen PES around third oxygen in the phosphorus-defective tetrahedral void (number 2 grey)

2. Another advantageous position of the third hydrogen atom can be observed, when hydrogen moved between two octahedral void (from num.6 black to num.5 black).
3. Generally, the more appropriate places of third hydrogen atom locations are the tetrahedral void (num.2 grey) and the octahedral void (num.5 black), which is confirmed by Table 3.6 after relaxation and non-relaxation information.

Table 3.6: Energy of hydrogen in different polyhedral sites around third oxygen

No	Initial → final	$\Delta E, \text{eV}$	No	Initial → final	$\Delta E, \text{eV}$
a	2oct → 2tet/3oct	0.000	h	3oct → 2tet/3oct	0.514
b	6oct → 5oct	0.190	k	3tet → 3oct	0.514
c	1oct → 2tet/4tet	0.511	l	4oct → 2tet/3oct	0.515
d	6tet → 2tet/3oct	0.512	m	8tet → 5oct	0.734
e	2tet → 2tet/3oct	0.512	n	5oct → 5oct	0.738
f	4tet → 2tet	0.512	o	7tet → 5oct	0.740
g	1tet → 1oct	0.514	p	5tet → 5oct	0.902

In Figure 3.19, the movement of third atom between initial and final positions is presented.

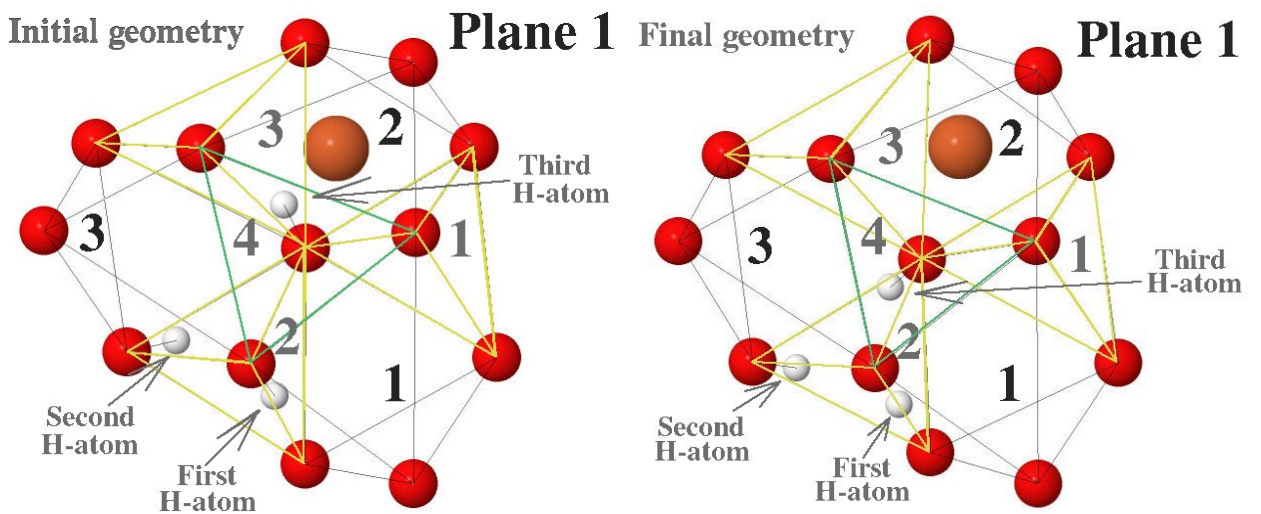


Figure 3.19: Hydrogen movement to stable position around third oxygen in phosphorus-defective LiFePO_4

3.3.4 PES for $\text{PO}_4/(\text{OH})_4$

The last stage of the substitution of phosphorus by four hydrogen defect investigation is presented in the Figure 3.20.

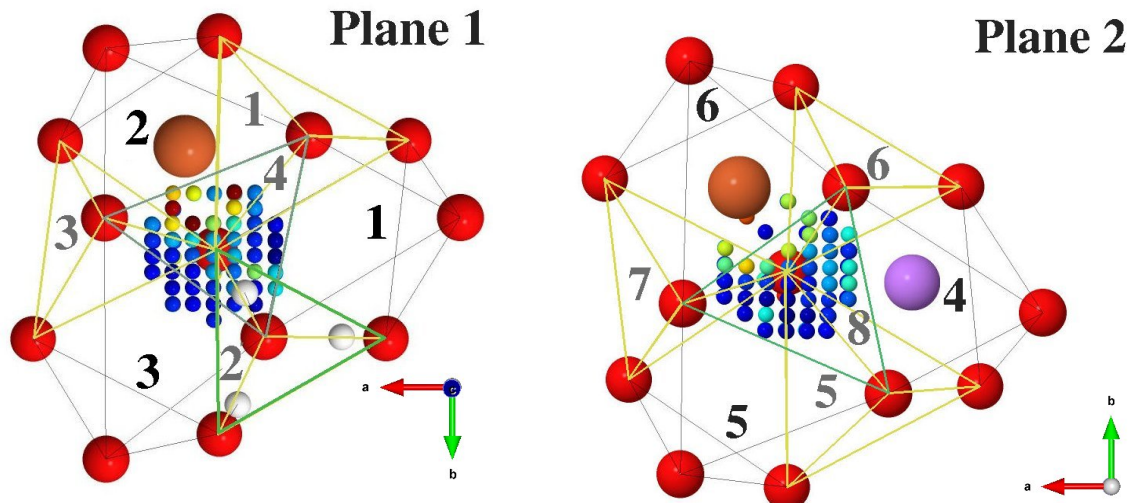


Figure 3.20: Hydrogen distribution around fourth oxygen in phosphorus-defective tetrahedral site (2 grey number)

According to the information about the formation energy of each hydrogen atom from Table 3.7, the conclusion about the place of appropriate hydrogen atom localization can be formulated. There are two octahedral sites (with 3 and 5 grey numbers), close to which the movement of the fourth hydrogen is advantageous.

Table 3.7: Energy of hydrogen in different polyhedra positions around fourth oxygen

No	Initial → final	$\Delta E, \text{eV}$	No	Initial → final	$\Delta E, \text{eV}$
a	3oct → 3oct	0.000	g	1tet → 4oct/5tet	0.184
b	5oct → 5oct	0.001	h	7tet → 3oct	0.307
c	5tet → 2tet/1oct	0.056	k	3tet → 3oct	0.309
d	4oct → 1oct	0.130	l	2tet → 2tet/1oct	0.921
e	8tet → 2tet/1oct	0.181	m	6tet/1oct	1.212
f	4tet → 4tet/2tet	0.181			

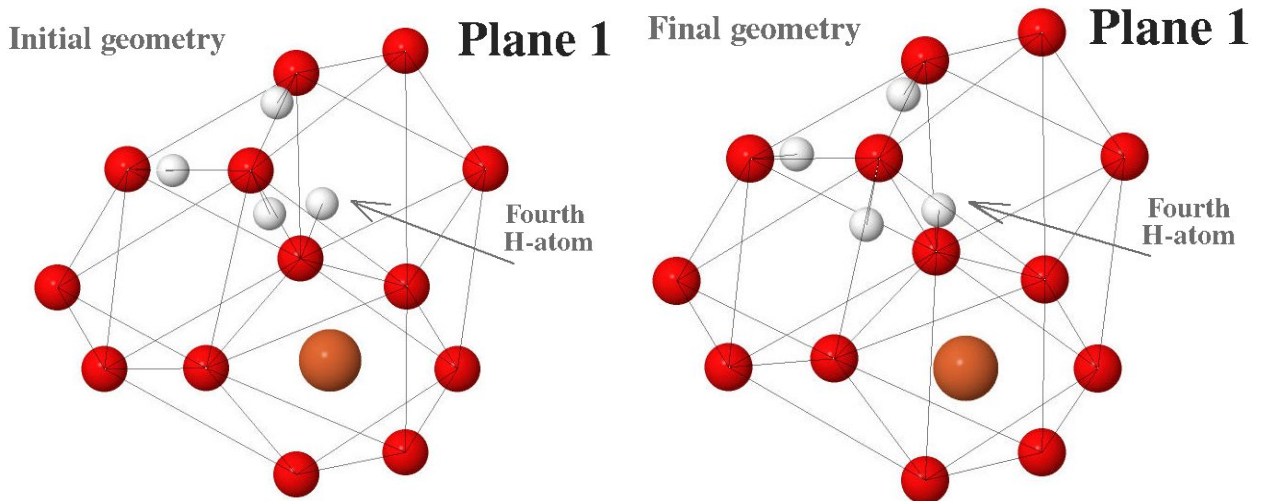


Figure 3.21: Hydrogen movement to stable position around fourth oxygen in phosphorus-defective LFP

Thus, the movement of the fourth hydrogen atom is presented in Figure 3.21 with corresponding between initial and final configuration of LiFePO_4 structure with phosphorus defect. The result of the calculation with atomic position relaxation shows the significant movement of the first hydrogen atom in comparison to its initial state. At the same time the fourth atom takes its place approximately along the O–O bond within phosphorus vacancy tetrahedron. As a result, the second, third, and fourth hydrogen atom under estimation took their place within the tetrahedron area of phosphorus vacancy site, while the first hydrogen atom localized in the neighboring octahedral void.

3.4 Formation energy of OH defects in LiFePO₄

As soon as the substitution of phosphorus by four hydrogen atoms defect structure was considered, its formation energy was compared with other defects, which were presented in previous sections. Additionally, if one phosphorus atom P⁵⁺ is removed from its stable position, five iron atoms in the neighboring area changes their oxidation state from Fe²⁺ to Fe³⁺. Then there can be two scenarios of substitution defects of phosphorus: four or five hydrogen atoms can be placed in the vacancy site, equation (3.6). Four atoms of hydrogen can build OH bonds with each of the oxygen in the tetrahedral environment. In this case just one iron atom will change its oxidation state. To achieve charge balance and taking into account the valency of a phosphorus atom in the crystal P⁵⁺ five atoms of hydrogen are needed. In this case all of the iron atoms will stay in their oxidation state equal to 2+. But, according to calculated energies, the last situation is less likely, Table 3.8.

$$E(P_{\text{vacancy}}) = \frac{1}{4}(E(LiFeP_{1-x}Vac_xO_4) - E(LiFePO_4) + \mu(P) - 4\mu(H)) \quad (3.6)$$

$$E(P_{\text{vacancy}}) = \frac{1}{5}(E(LiFeP_{1-x}Vac_xO_4) - E(LiFePO_4) + \mu(P) - 5\mu(H))$$

Some small changes of atom positions have been happening in the structure during the calculation with atomic positions relaxation. The comparison between two possible substitution defects are presented in Figure 3.22. For LiFePO₄ with phosphorus vacancy and four hydrogen atoms as an impurity the distances between hydrogen and neighboring oxygen are: (O-H)₁ = 0.97 Å, (O-H)₂ = 1.00 Å, (O-H)₃ = 1.00 Å, (O-H)₄ = 0.98 Å. In case of substitution of phosphorus by five hydrogen: (O-H)₁ = 0.98 Å, (O-H)₂ = 1.01 Å, (O-H)₃ = 1.01 Å, (O-H)₄ = 0.97 Å, (O-H)₅ = 1.04 Å.

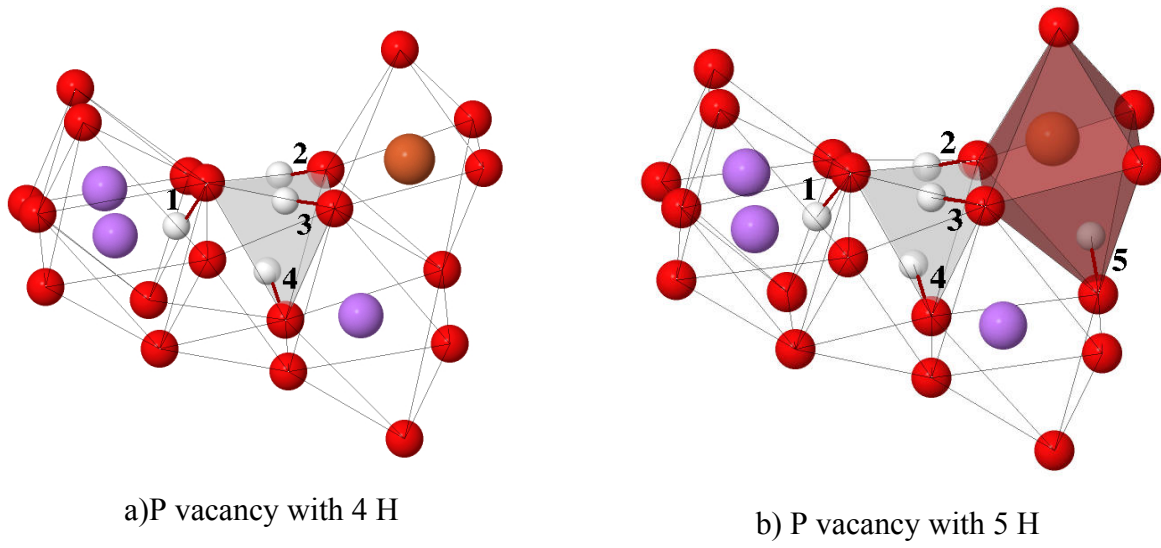


Figure 3.22: Substitution of phosphorus by hydrogen after structural optimization

Table 3.8: Characteristics of P/4H and P/5H defects

Type	Bonds	Distance, Å	E_{form}, eV (GGA) $\mu(O_2)=-11.52\text{eV}$	E_{form}, eV (GGA) $\mu(O_2)=-13.1\text{eV}$	E_{form}, eV (GGA+U) $\mu(O_2)=-13.1\text{eV}$
4 hydrogen in P vacancy site	$(O-H)_1$ $(O-H)_2$ $(O-H)_3$ $(O-H)_4$	0.97 1.00 1.00 0.98	0.56	0.51	0.53
5 hydrogen in P vacancy site	$(O-H)_1$ $(O-H)_2$ $(O-H)_3$ $(O-H)_4$ $(O-H)_5$	0.98 1.01 1.01 0.97 1.04	0.93	0.89	0.73

According to the knowledge about the formation energies of different defect types the conclusion about more preferable substitution of phosphorus by four hydrogen defects can be made. According to Table 3.3 and 3.8 the formation energy values for the substitution of lithium by one hydrogen, iron by two hydrogen, and phosphorus by five hydrogen increase with decreasing of the oxygen chemical potential. At the same time, the formation energy of the phosphorus substitution by four hydrogen decreases with the decrease of oxygen chemical potential. Such behavior corresponds to a more efficient substitution of phosphorus by four hydrogen defects in the experimental conditions.

3.5 Molecular dynamic simulation

Molecular dynamic simulations were performed at several fixed temperatures: 690 K, 890 K, and 1390 K. These values were chosen according to the annealing temperatures in experimental synthesis conditions: low temperature 690 K (400°C) is not enough to achieve the crystallinity and enhance the electrochemical reactivity of the sample. The temperature of approximately 890 K (600°C) is used in the synthesis conditions, while 1390 K (1100°C) is used in the annealing process.

The evolution of the system with 25% of $\text{PO}_4/(\text{OH})_4$ defects at elevated temperatures of 400°C and 600°C shows the fluctuation of hydrogen positions around corresponding oxygen. The covalent O-H bond, which was discovered from PES study, has been keeping during the molecular dynamic simulation. This behavior is presented in the statistical distribution of O-H bond distance over the 2 ps time slot, Figure 3.23. Here the each color of points (red, green, yellow, blue) corre-

spond to each of the four OH groups. The fluctuation of O-H-O angle is presented in Figure 3.24. The absence of a hydrogen bond can be concluded due to the strong deviation of O-H-O angle from 180° value.

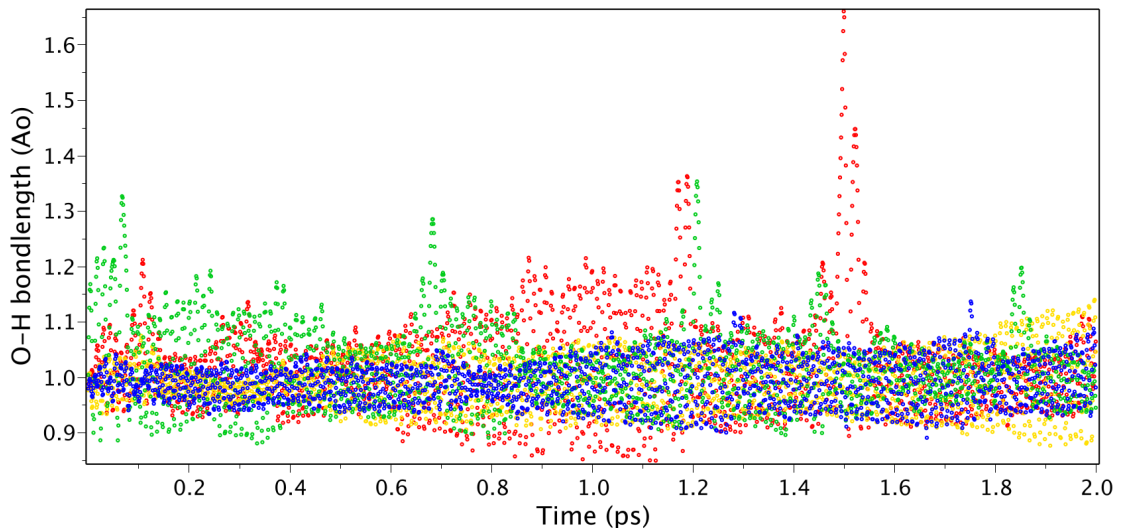
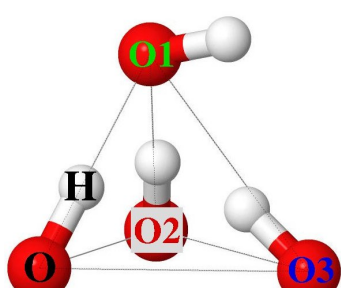
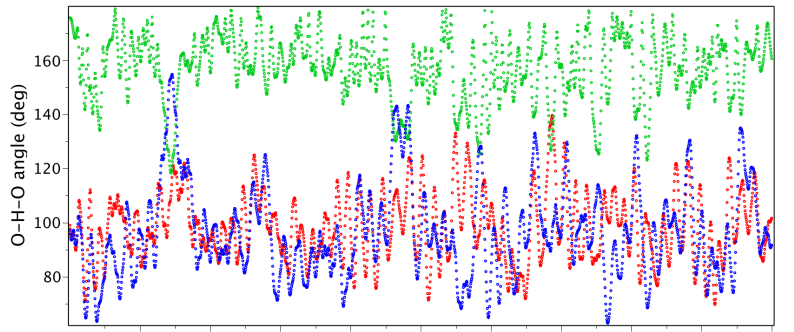


Figure 3.23: The evolution of O-H distance over time at 600°C . Each color is corresponded to each of the four OH groups in the tetrahedron.



a)Structure of $\text{PO}_4/(\text{OH})_4$ under MD study



b)Fluctuation of O-H-O angles over the time

Figure 3.24: a) The schematic view of $\text{PO}_4/(\text{OH})_4$ defect and b) distribution of O-H-O angles over time; the O-H-O1 angle is green line, O-H-O2 angle is red line, and O-H-O3 angle is blue line.

The molecular dynamic simulation of $\text{PO}_4/(\text{OH})_4$ defect with 6.25% concentration at 600°C shows temporal formation of H_2 molecule. The distribution of O-H bond distances between the selected hydrogen atom (H in the Figure 3.25 a)) and neighboring oxygen atoms is presented in the Figure 3.25. The unbound free-floating hydrogen atom are not observed. Each hydrogen atom either creates a bond with the oxygen atom or it forms a bond with another hydrogen.

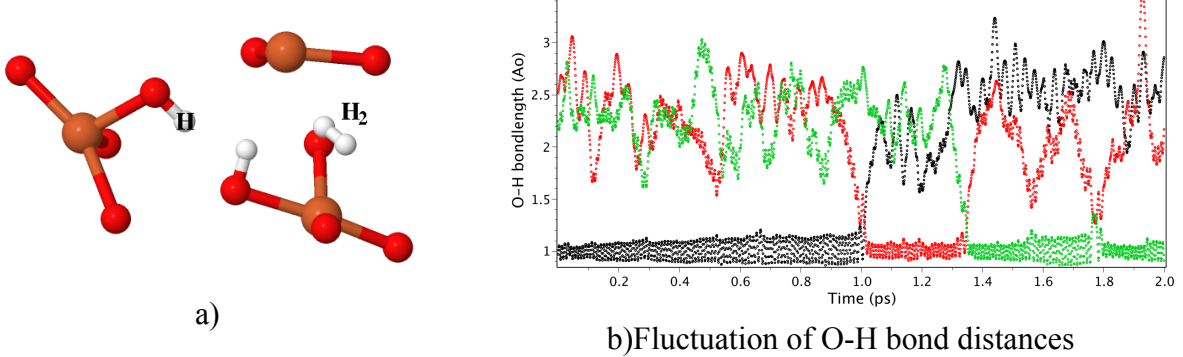


Figure 3.25: a) A snapshot of $\text{PO}_4/(\text{OH})_4$ defect with H_2 molecule inside. b) The distribution of O-H distances over time: O-H is black line, O1-H is green line, and O2-H is red line.

The H-H bond length shows bimodal distribution with two peaks centered at 0.7 \AA and 0.85 \AA (Figure 3.26). The corresponded view of H-H bond is presented in Figure 3.27 a). No stable Fe-H bond was obtained as an equilibrium over time. Thus, the configuration presented in Figure 3.27 b) is unstable.

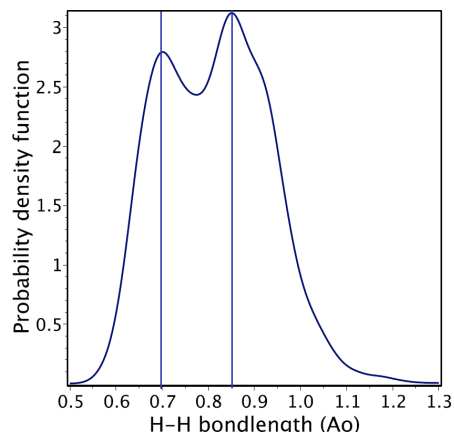


Figure 3.26: The statistical distribution of H-H distance

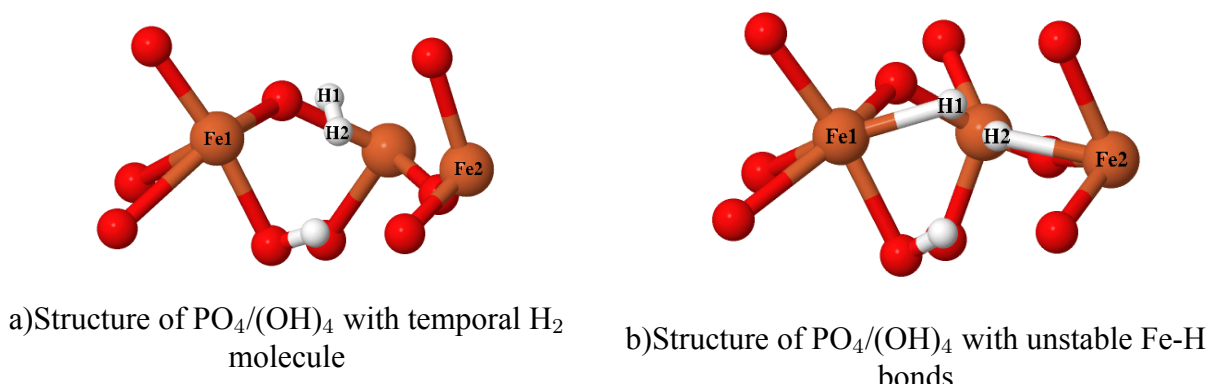


Figure 3.27: The schematic view of $\text{PO}_4/(\text{OH})_4$ defect with a) 0.7 \AA of H-H bond; b) 0.85 \AA of H-H bond.

Additionally, the molecular dynamic search of LiFePO₄ with 25% of PO₄/(OH)₄ concentration was provided at high temperature of 1100°C. This abnormally high temperature allows to consider a larger configuration space of possible states without the increase in simulation time. The result of such molecular dynamic investigation shows formation of unstable water molecule (Figure 3.28).

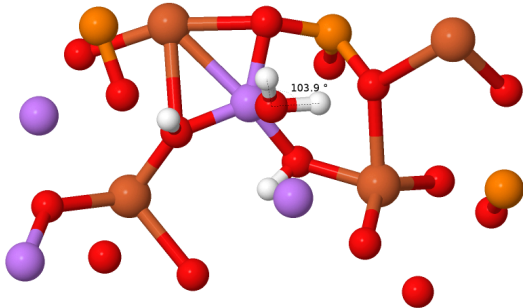


Figure 3.28: The snapshot showing H₂O molecule formation during MD simulation at 1100°C

3.6 Structure of PO₄/(OH)₄ defect in LiFePO₄ and LiMnPO₄

After potential energy scan of possible OH defects and its molecular dynamic simulation the structures with the lowest energies were selected (Figure 3.29).

The stable structure of LiFePO₄, which was considered in PES scan, is presented in Figure 3.29 b). Its unit cell total energy is equal to -202.5 eV after relaxation of atomic positions. This structure configuration was used in the molecular dynamic search at 600°C. According to that results the two additional low-energy stable configurations were obtained. One of them has slightly lower energy -202.51 eV in comparison with the initial structure, Figure 3.29 a), and one with much larger energy -201.28 eV, Figure 3.29 c). In the case of LiFePO₄ the MD study allowed to find more stable PO₄/(OH)₄ configuration.

The LiMnPO₄ structure with PO₄/(OH)₄ defect considered after PES study is presented in the Figure 3.29 d). This configuration has -209.32 eV energy per unit cell after atomic relaxation. It was investigated in the molecular dynamic simulation at 600°C. Two more stable configurations of PO₄/(OH)₄ were found, Figure 3.29 e) and f) with slightly higher energy of the unit cell in comparison with the initial structure.

The combination of PES method and MD simulations with subsequent relaxation of atomic positions at 0K proves to be a good method for finding the most stable structure of PO₄/(OH)₄ defect.

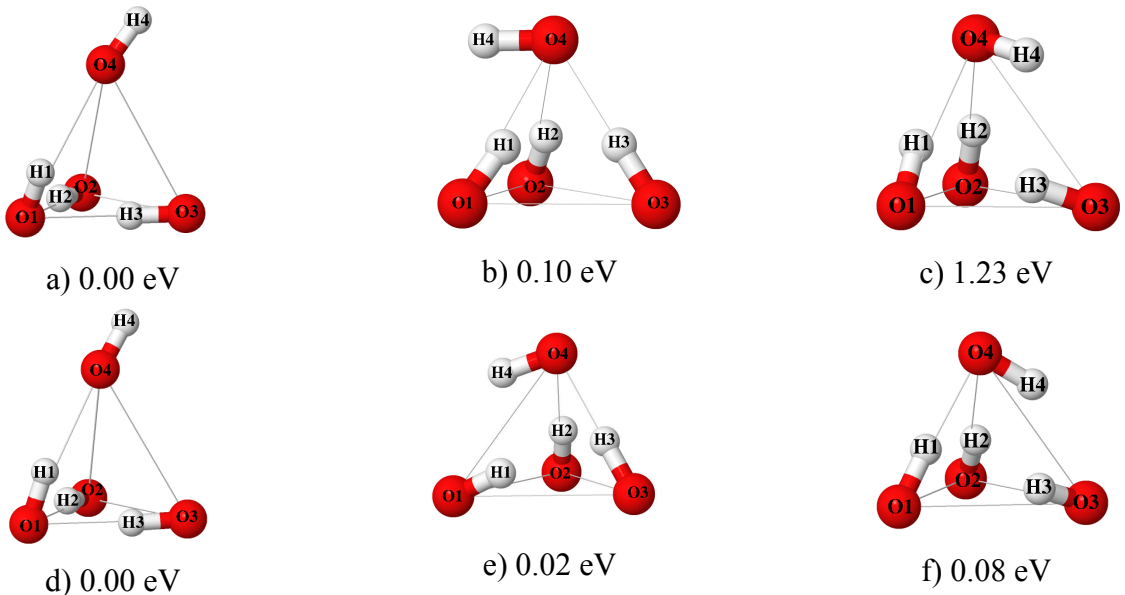


Figure 3.29: Structure and energy of of $\text{PO}_4/\text{O}_4\text{H}_4$ defect in a-c) LiFePO_4 and d-f) LiMnPO_4

3.7 Electronic properties of defective structures

The influence of the phosphorus vacancy and OH defects on the electronic properties of the material was investigated in the current work. The main disadvantage of LiFePO_4 and LiMnPO_4 is their poor electronic conductivity in the pure form. The carbon coating is used at the sample preparation stage to solve this problem. Thus, the improvement of electronic properties of material is a crucial aim of its preparation. Moreover, the electronic conductivity can be affected by hydroxyl group defects due to the charge compensation mechanism [1].

Firstly, the influence of phosphorus vacancy on the electronic structure was considered by calculating total density of states (Figure 3.30). In the case of P vacancy the spin up states appear at Fermi level in addition to spin down states observed for ideal LiFePO_4 (Figure 3.30).

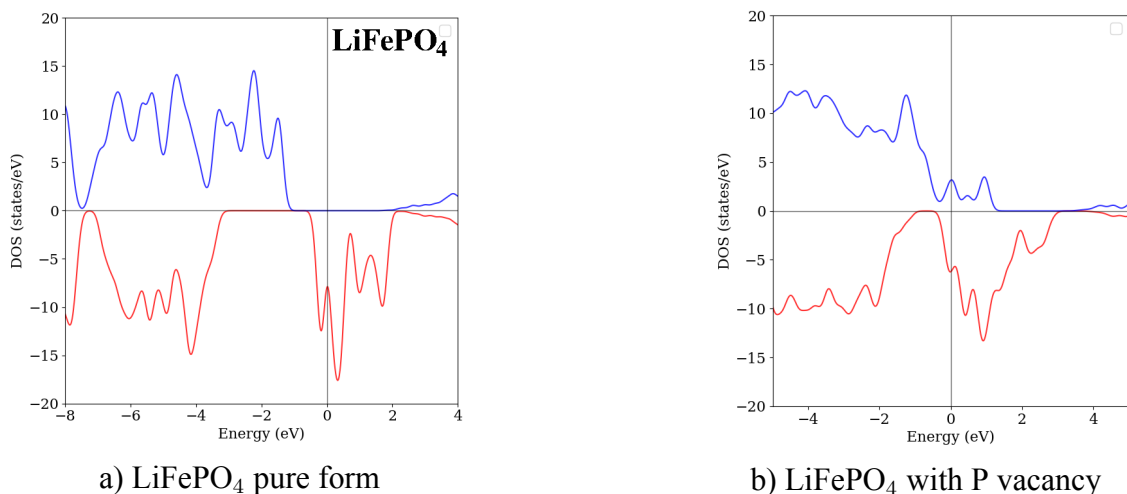


Figure 3.30: Calculated total density of states of a) pure LiFePO_4 and b) LiFePO_4 with P vacancy

The influence of substitution of phosphorus by one and two hydrogen is presented in the Figure 3.31 a) and b), where no significant changes compared to the single P vacancy are seen. Density of states of LiFePO₄ material with substitution of phosphorus by three and four hydrogen is shown in the Figure 3.32 a) and b), respectively. Here more significant changes of DOS are seen with slight increase of density at Fermi level. The absence of band-gap at the Fermi level is seen in this case.

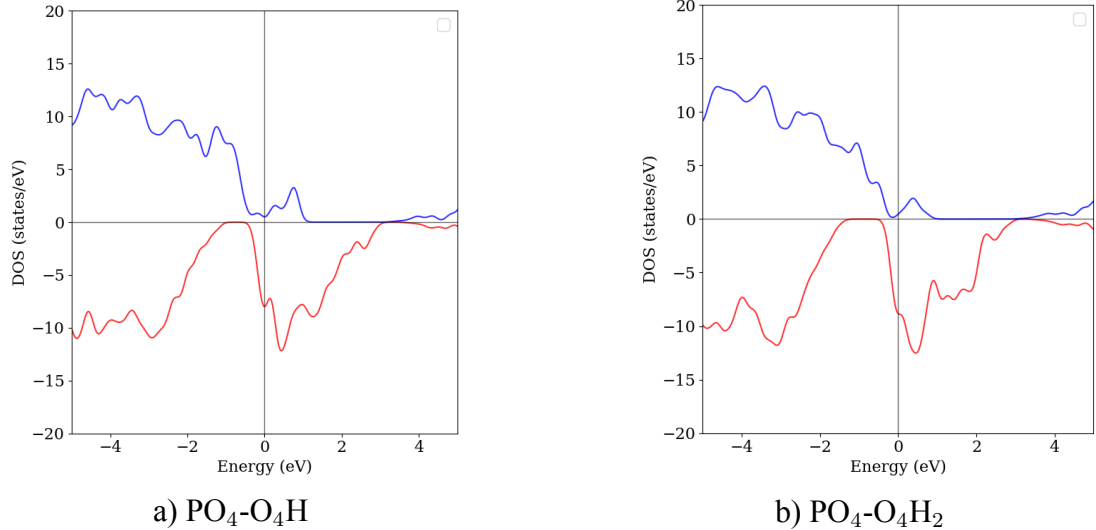


Figure 3.31: DOS of LiFePO₄ with different defect composition

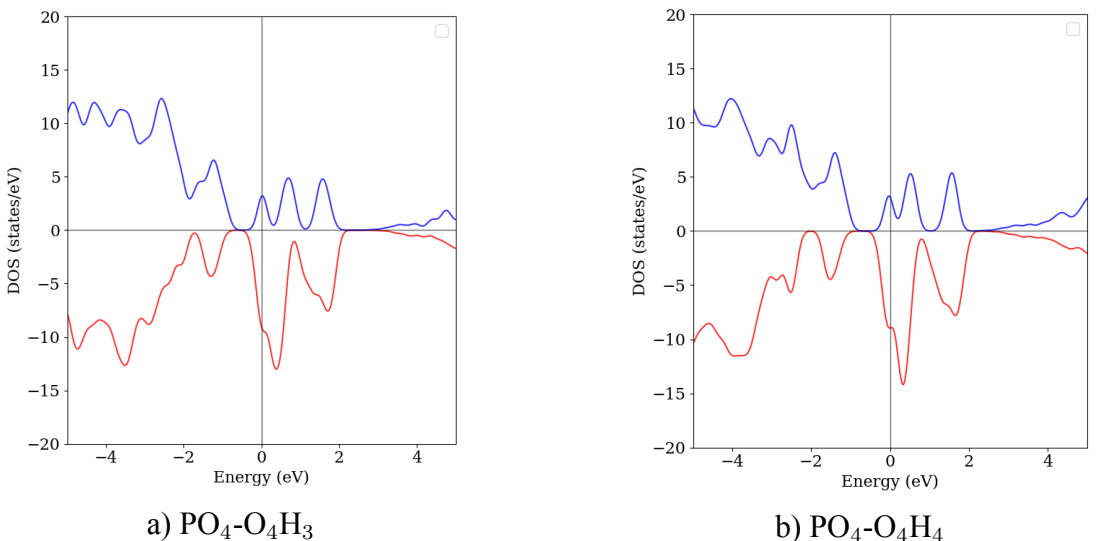


Figure 3.32: DOS of LiFePO₄ with different defect composition

The same calculations of DOS were repeated in the case of hydroxyl group defects existing in LiMnPO₄ (Figure 3.33). When the density of states of pure LiMnPO₄ shows the absence of states at the Fermi level and the presence of 2.1 eV energy gap (Figure 3.33 a)), while the phosphorus defective structure shows the presence of the electronic states at the Fermi level, Figure 3.33 b). The influence of 1, 2, 3 or 4 hydrogen substitution atom in place of defective PO₄ is presented in

Figure 3.34 a)-d), respectively. In these cases little differences compared to single P vacancy are observed.

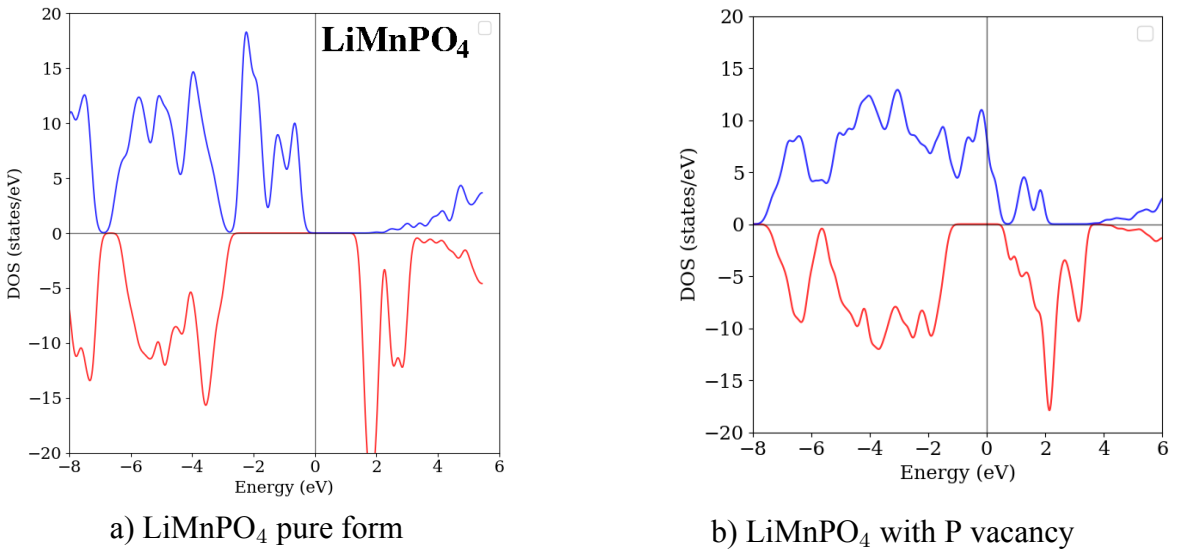


Figure 3.33: Calculated total density of states of a) pure LiMnPO₄ and b) LiMnPO₄ with P vacancy

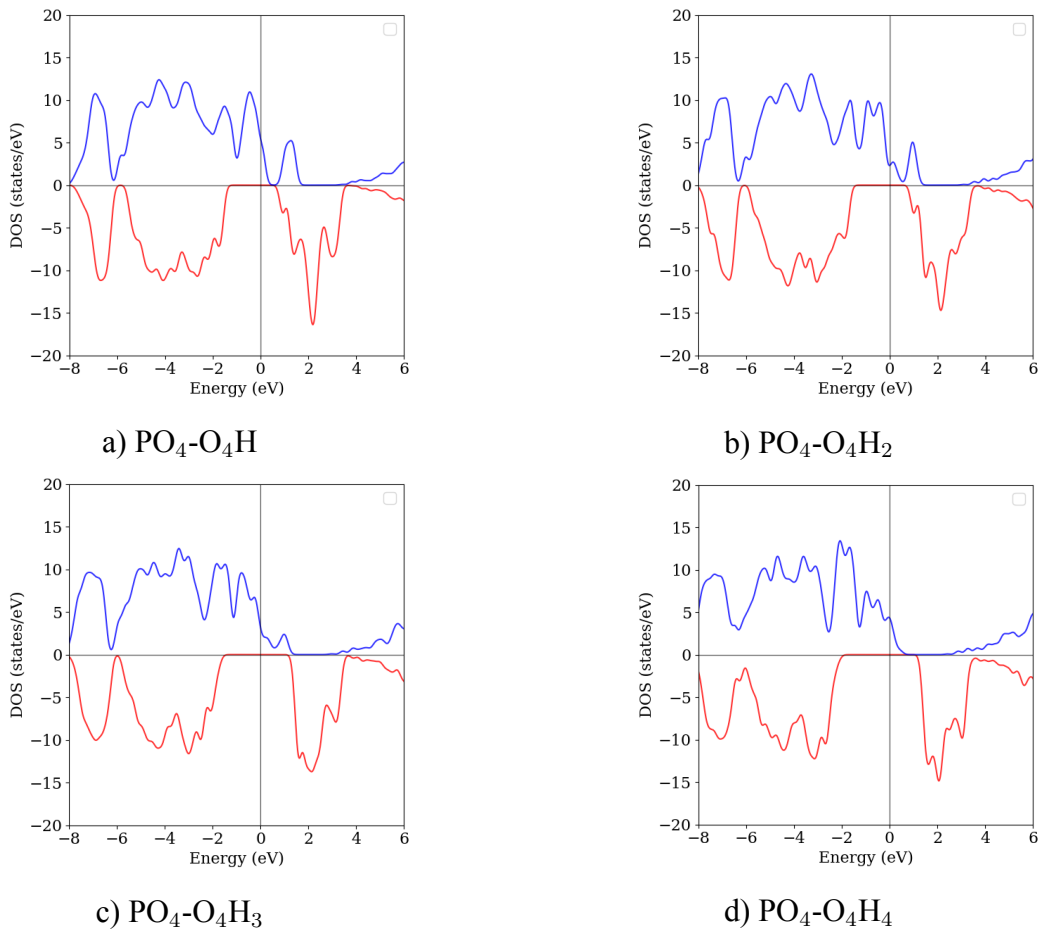


Figure 3.34: DOS of LiMnPO₄ with different defect composition

It should be noted that total density of states is not well suited for studying the influence of point defects on electronic structure. Moreover, as it was shown in the beginning, the GGA

without U does not reproduce the band gap in agreement to experimental results. Therefore, we plan to calculate partial density of states using GGA+U approach in our future work.

3.8 Discussion

Despite the widely used lithium-ion batteries based on LiFePO₄ cathode material, the investigation of OH defect in this material is highly relevant. The main aim of the current work was to determine the structure and energetics of OH defects in Li(Fe,Mn)PO₄ compounds using computational tools based on density functional theory.

The computational methods based on density functional theory was used to study the energetics and structure of OH defects in LiFePO₄ and LiMnPO₄ cathode compounds. By performing a full potential energy surface scan the atomic structure of PO₄/(OH)₄ defect was found. This structure is in good agreement with similar defect in a forsterite material Mg₂SiO₄ [40], where OH defects were investigated in details.

The combination of PES scan with *ab initio* molecular dynamics constitutes the good tool of consistent defect structure study. Nevertheless, a longer molecular dynamics runs are required to provide more information on possible structural transformations of OH-defects in LiFePO₄ material at temperatures relevant for experiment.

Additionally, the study of electronic properties of LiFePO₄ and LiMnPO₄ materials with more sophisticated methods is required. The usage of the Hubbard correction is required in order to take into account the localization of d-electrons.

Conclusions

The study of OH defects in LiFePO₄ and LiMnPO₄ compounds was performed with density functional theory (DFT) and ab initio molecular dynamics. The energy and structure of interstitial H as well as substitutional Li/H, Fe/2H, and PO₄/(OH)₄ defects were calculated with DFT and DFT+U methods. It is shown that the DFT+U method is required for the correct reproduction of electronic structure and formation energies, while DFT without U method can be used for calculating the structure of defects.

In the case of PO₄/(OH)₄ defect full scan of potential energy surface was performed and allowed to find the lowest-energy structural configurations of this defect. According to the developed thermodynamic model and DFT+U results the PO₄/(OH)₄ defect has the lowest formation energy per hydrogen atom among all considered defects. In PO₄/(OH)₄ defect four hydrogen atoms form covalent O–H bonds with 1 Å bond length. Three O–H bonds are directed inside the O₄-tetrahedral void left after phosphorus atom removal, while the fourth O–H is located in the neighborhood tetrahedral void.

The *ab initio* molecular dynamics showed that the PO₄/(OH)₄ defect remains localized at temperatures up to 1100°C emphasizing its strong trapping to P vacancy. At the same time, local rearrangements of H atoms inside the defect are observed at much lower temperatures. In particular, the temporal formation of H₂ molecule with a bimodal distribution of H-H bond length (0.7 and 0.85 Å) was observed inside PO₄/(OH)₄ defect at 600°C. At 1100°C the temporal formation of H₂O molecule with distorted H-O-H angles inside PO₄/(OH)₄ defect was also discovered.

Overall, the current study provides insights into the structure and dynamics of OH defects, which is required for further studies of their influence on materials properties. The revealed dependencies of OH formation energies on oxygen chemical potential may help to rationalize the synthesis procedure of LiFePO₄ cathode material and reduce the concentration of detrimental OH defects.

Appendix A

Program code

A.1 Potential Energy Surface method

```
def PES_scan(submit = 0, cl = None, a = None, b = None, readfiles = 1):
    """
    Create spherical PES around oxygen for H

    INPUT:
        submit (bool) - 1 - run add() and submit to cluster, 0 - run res()
        cl = initial structure
        a = min of O-H distance
        b = max of O-H distance

    RETURN:
        namelist - list of calculation names
    """

    sc = cl.end
    sc_Hrep = copy.deepcopy(sc)
    sc_Hall = copy.deepcopy(sc)
    R = sc.rprimd
    R1n = np.linalg.norm(R[0])
    R2n = np.linalg.norm(R[1])
    R3n = np.linalg.norm(R[2])

    # function for choosing the atom:
    xO1 = cl.init.xred[18] # i used O position from initial
    xO1c= sc.xcart[18]
    'z = ', xO1[2], '\nParemetres of uc: ', 'a = ', R1n, 'b = ', R2n, 'c = ', R3n
    #For first atom
    # x_list = [num / 100 for num in range(int(round((xO1[0] - 0.3)*100)),
    # int(round((xO1[0] + 0.4)*100)), 3)]
    # y_list = [numy / 100 for numy in range(int(round((xO1[1] - 0.3)*100)),
    # int(round((xO1[1] + 0.4)*100)), 3)]
```

```

# z_list = [numz / 100 for numz in range(int(round((xO1[2] - 0.3)*100)),
int(round((xO1[2] + 0.4)*100)), 4)]
num=0
namelist = []
for i, x in enumerate(x_list):
    for j, y in enumerate(y_list):
        for k, z in enumerate(z_list):
            d=math.sqrt(math.pow((x-xO1[0])*R1n, 2) +
            +math.pow((y-xO1[1])*R2n, 2)+math.pow((z-xO1[2])*R3n,2))
            if (d >= a and d <= b):
                num+=1
                xH = xred2xcart([np.array([x, y, z])],R)[0]
                d1, d2 = image_distance(xH, xO1c, R)
                print( 'Distances are: {:.3.2f} {:.3.2f}'.format(d1, d))
                sc_Hijk = sc_Hrep.add_atom([x / 1, y / 1, z / 1], 'H')
                sc_Hall = sc_Hall.add_atom([x / 1, y / 1, z / 1], 'H')
                id = (str(num)+"LFP"+"-"+str(i)+"-"+str(j)+"-"+str(k),
'0', 1)
                if submit:
                    add(*id, up = 'up2', input_st = sc_Hijk, it_folder =
                    'LFP_scan_O4/', cluster='pardus', corenum=4)
                else:
                    res(*id, up = 'up2', show = 'fo', readfiles = readfiles)
                    # try show = 'en', 'conv', 'est'
                namelist.append(id)
sc_Hall.name+='Hall'
sc_Hall.write_poscar()
return namelist

```

A.2 Solution energies calculation

```

def calc_solution_energies(namelist, inum_of_H=0, num_of_H=1,
                           cl_ref = None, shift = None):

```

namelist - list of calculation names

cl_ref - initial structure (with (n-1) number of hydrogens)

shift - a vector of atoms shift

Calculate energy of Hydrogen solution in:

inum_of_H - number of hydrogen in the initial structure,

num_of_H - general number of hydrogens in structure under calculation

""""

```
chem_pot_0 = LFPtet1.e0 - LFP122.e0
```

```
dmulist = []
```

```
xlist = []
```

```
energies = []
```

```
first_calculation = db[namelist[0]]
```

```
z = 1 #Hydrogen
```

```
list_of_positions_of_atoms = first_calculation.end.get_specific_elements([z])
```

```
i = list_of_positions_of_atoms[inum_of_H] # hydrogen number in lists
```

```
print (i)
```

```
for name in namelist:
```

```
    dmulist.append( db[name].e0 - cl_ref.e0 - chem_pot_0)
```

```
    energies.append(db[name].e0)
```

```
    st = db[name].end
```

```
    if shift is not None:
```

```
        st = st.shift_atoms(shift)
```

```
        xlist.append(st.xcart[i] )
```

```
    st_ref = cl_ref.end.copy()
```

```
    if shift is not None:
```

```
        st_ref = st_ref.shift_atoms(shift)
```

```
return dmulist, xlist, st_ref, energies
```

A.3 Juxtaposition between color and energy of each hydrogen position

```
def energy2color(elist, energies, cmap = None):
```

""""

INPUT:

elist - list of energy differences

energies - list of structure energy (with n number of hydrogen)

cmap (str) - color map according www.map...

```

#####
colors = []
max_val = max(energies)
min_val = min(energies)
print('MAX_VALUE', max_val, '\nMIN VALUE', min_val)
norm = mpl.colors.Normalize(vmin=min_val, vmax=max_val)
# to normalize data from 0.0 (vmin) to 1.0 (vmax)
m = cm.ScalarMappable(norm=norm, cmap=mpl.cm.jet)
# RGBA colors to normalization
map_to_color = np.vectorize(m.to_rgba)
for e in elist:
    color = mpl.colors.rgb2hex( map_to_color( e ) )
    colors.append( color )
return colors

```

A.4 To reduce the extreme energy values

```
def modify(dmulist, xlist, namelist, mucut=2, mucut1=-10):
```

```
#####

```

```
to deletet the points with energies more than mucut
```

```
#####

```

```

new_dmulist = []
new_xlist = []
new_namelist = []
for dmu, x, n in zip(dmulist, xlist, namelist):
    if dmu < mucut:
        if dmu > mucut1:
            new_dmulist.append(dmu)
            new_xlist.append(x)
            new_namelist.append(n)

```

```
new_xlist_n = []
```

```
k=0
```

```
for n in range(len(new_xlist)):
```

```
    k+=1
```

```
    new_xlist_n = new_xlist[n]
```

```
return new_dmulist, new_xlist, new_namelist
```

A.5 To create the jmol script to visualize the full hydrogen distribution

```
def write_jmol_script(st, colors, xlist, local_path, num_of_H=0,
                      shift = None, shift1 = None):
    jmolfie = '/home/irina/LFP/LFP_scan_O4/file/Henergy4.jmol'
    stH = st.add_atoms(xlist, 'H')
    if shift:
        stH = stH.shift_atoms(shift)
    if 0:
        filename = stH.write_poscar()
    else:
        filename, png = stH.write_xyz(path = '/home/irina/LFP/LFP_scan_O4/file')
        stH.write_poscar()
    list_of_positions_of_atoms = stH.get_specific_elements([1])
    i = list_of_positions_of_atoms[num_of_H]
    print(i)
    print(st.natom)
    print(list_of_positions_of_atoms)
    basename = os.path.basename(filename)
    if local_path:
        filename = local_path + '/' + basename
    colors_jmol = [c.replace('#', 'x') for c in colors]
    with open(jmolfie, 'w') as f:
        f.write('set frank off \nset autobond off \n')
        f.write('load "'+filename+'"\n')
        f.write('select H* \ncpk 30 \n')
        f.write('set displayCellParameters False ; \n ')
        for i in range(len(xlist)):
            f.write('select atomno = '+str(i+st.natom+1)+'\n')
            # f.write('select atomno = '+str(i+2)+'\n')
            f.write('color ['+colors_jmol[i]+'];\n ')
        xlist = [stH.xcart[i] for i in list_of_positions_of_atoms]
        xc = sum(xlist)/len(xlist)
        print(xc)
```

```
stH = stH.copy()
# stH= replic(stH, (2, 2, 2))
if shift1 is not None:
    stH = stH.shift_atoms(shift1)
# stH = stH.return_atoms_to_cell()
for i, x in enumerate(stH.xcart):
    d1, d2 = image_distance(xc, x, stH.rprimd)
    if d1>10:
        f.write('select atomno = '+str(i+1)+'; cpk 0\n')
return jmolfie
```

Bibliography

- [1] Vasily D Sumanov, Dmitry A Aksyonov, Oleg A Drozhzhin, Igor Presniakov, Alexey V Sobolev, Iana Glazkova, Alexander A Tsirlin, Dmitry Rupasov, Anatoliy Senyshyn, Irina V Kolesnik, et al. “Hydrotriphylites” $\text{Li}_{1-x}\text{Fe}_{1+x}(\text{PO}_4)_{1-y}(\text{OH})_4y$ as cathode materials for li-ion batteries. *Chemistry of Materials*, 31(14):5035–5046, 2019.
- [2] Linden David and B Reddy Thomas. Handbook of batteries, 2001.
- [3] GX Wang, Y Chen, K Konstantinov, Matthew Lindsay, HK Liu, and SX Dou. Investigation of cobalt oxides as anode materials for li-ion batteries. *Journal of Power Sources*, 109(1):142–147, 2002.
- [4] Raffael Ruess, Sebastian Haas, Andreas Ringleb, and Derck Schlettwein. Dye-sensitized solar cells with electrodeposited ZnO and Co(bpy)₃ redox electrolyte: Investigation of mass transport in the electrolyte and interfacial charge recombination. *Electrochimica Acta*, 258:591–598, 2017.
- [5] Shu Luo, Ke Wang, Jiaping Wang, Kaili Jiang, Qunqing Li, and Shoushan Fan. Binder-free LiCoO_2 carbon nanotube cathodes for high-performance lithium ion batteries. *Advanced Materials*, 24(17):2294–2298, 2012.
- [6] Soo Seok Choi and Hong S Lim. Factors that affect cycle-life and possible degradation mechanisms of a Li-ion cell based on licoo_2 . *Journal of Power Sources*, 111(1):130–136, 2002.
- [7] K Amine, H Yasuda, and M Yamachi. Olivine LiCoPO_4 as 4.8 v electrode material for lithium batteries. *Electrochemical and Solid-State Letters*, 3(4):178–179, 2000.
- [8] Hongwei Yan, Xuejie Huang, and Liquan Chen. Microwave synthesis of LiMn_2O_4 cathode material. *Journal of power sources*, 81:647–650, 1999.
- [9] PMW Salehen, H Razali, K Sopian, TK Lee, and MS Su’ait. Evaluation of charge-discharge characteristic of lithium cobalt nickel manganese oxide for high-energy density lithium-ion batteries. *Journal of the Society of Automotive Engineers Malaysia*, 1(3), 2017.
- [10] Kelimah Elong, Norlida Kamarulzaman, Roshidah Rusdi, Nurhanna Badar, and Mohd Hilmi Jaafar. Solid solutions of $\text{LiCo}_{1-x}\text{Ni}_x\text{O}_2$ ($x = 0, 0.1, \dots, 0.9$) obtained via a combustion synthesis route and their electrochemical characteristics. *ISRN Condensed Matter Physics*, 2013, 2013.

- [11] Junli Sun, Wenxiu Peng, Dawei Song, Qinghong Wang, Hongmei Du, Lifang Jiao, Yuchang Si, and Huatang Yuan. Electrochemical properties of facile emulsified LiV₃O₈ materials. *Materials Chemistry and Physics*, 124(1):248–251, 2010.
- [12] Yongmei Liu, Xuechou Zhou, and Yonglang Guo. Effects of fluorine doping on the electrochemical properties of LiV₃O₈ cathode material. *Electrochimica acta*, 54(11):3184–3190, 2009.
- [13] AK Padhi, KS Nanjundaswamy, C Masquelier, Shigeto Okada, and John B Goodenough. Effect of structure on the Fe³⁺/Fe²⁺ redox couple in iron phosphates. *Journal of the Electrochemical Society*, 144(5):1609, 1997.
- [14] Sylvain Franger, Frederic Le Cras, Carole Bourbon, and Helene Rouault. Comparison between different LiFePO₄ synthesis routes and their influence on its physico-chemical properties. *Journal of Power Sources*, 119:252–257, 2003.
- [15] Vanchiappan Aravindan, Joe Gnanaraj, Yun-Sung Lee, and Srinivasan Madhavi. LiMnPO₄ – a next generation cathode material for lithium-ion batteries. *Journal of Materials Chemistry A*, 1(11):3518–3539, 2013.
- [16] Atsuo Yamada, Yuki Takei, Hiroshi Koizumi, Noriyuki Sonoyama, Ryoji Kanno, Keiji Itoh, Masao Yonemura, and Takashi Kamiyama. Electrochemical, magnetic, and structural investigation of the Li_x(Mn_yFe_{1-y})PO₄ olivine phases. *Chemistry of materials*, 18(3):804–813, 2006.
- [17] Denis Arčon, Andrej Zorko, Robert Dominko, and Zvonko Jagličić. A comparative study of magnetic properties of LiFePO₄ and LiMnPO₄. *Journal of Physics: Condensed Matter*, 16(30):5531, 2004.
- [18] Xiaoyue Xu, Tao Wang, Yujing Bi, Meng Liu, Wenchao Yang, Zhe Peng, and Deyu Wang. Improvement of electrochemical activity of LiMnPO₄–based cathode by surface iron enrichment. *Journal of Power Sources*, 341:175–182, 2017.
- [19] NV Urusova, MA Semkin, S Lee, Yu A Barykina, DG Kellerman, AE Teplykh, AN Pirogov, AS Volegov, and Yu N Skryabin. Magnetic ordering and crystal structure of LiMPO₄ compounds with M=(Mn, Fe, Ni/Mn, and Ni/Co). *Ferroelectrics*, 509(1):74–79, 2017.
- [20] DA Aksyonov, SS Fedotov, KJ Stevenson, and A Zhugayevych. Understanding migration barriers for monovalent ion insertion in transition metal oxide and phosphate based cathode materials: A dft study. *Computational Materials Science*, 154:449–458, 2018.

- [21] Shyue Ping Ong, Vincent L Chevrier, and Gerbrand Ceder. Comparison of small polaron migration and phase separation in olivine LiMnPO_4 and LiFePO_4 using hybrid density functional theory. *Physical Review B*, 83(7):075112, 2011.
- [22] Guofeng Zhou and Shuaiyang Guo. Comparative study on hydrothermally synthesized $\text{LiMn}_{x}\text{Fe}_{1-x}\text{PO}_4$ ($x=0\sim 1$) cathode at full-cell level. *Russian Journal of Applied Chemistry*, 90(7):1188–1192, 2017.
- [23] Borong Wu, Yonghuan Ren, and Ning Li. LiFePO_4 cathode material, electric vehicles—the benefits and barriers, dr. seref soylu (ed.), isbn: 978-953-307-287-6, intech, 2015.
- [24] H Huang, S-C Yin, and LF s Nazar. Approaching theoretical capacity of LiFePO_4 at room temperature at high rates. *Electrochemical and Solid-State Letters*, 4(10):A170–A172, 2001.
- [25] Keisuke Shiraishi, Kaoru Dokko, and Kiyoshi Kanamura. Formation of impurities on phospho-olivine LiFePO_4 during hydrothermal synthesis. *Journal of power Sources*, 146(1-2):555–558, 2005.
- [26] K Zaghib, A Mauger, John B Goodenough, F Gendron, and CM Julien. Electronic, optical, and magnetic properties of LiFePO_4 : small magnetic polaron effects. *Chemistry of materials*, 19(15):3740–3747, 2007.
- [27] Hongliang Zhang, Yang Gong, Jie Li, Ke Du, Yanbing Cao, and Jiaqi Li. Selecting substituent elements for LiMnPO_4 cathode materials combined with density functional theory (dft) calculations and experiments. *Journal of Alloys and Compounds*, 793:360–368, 2019.
- [28] M Saiful Islam, Daniel J Driscoll, Craig AJ Fisher, and Peter R Slater. Atomic-scale investigation of defects, dopants, and lithium transport in the LiFePO_4 olivine-type battery material. *Chemistry of Materials*, 17(20):5085–5092, 2005.
- [29] Andrea Paoletta, Giovanni Bertoni, Pierre Hovington, Zimin Feng, Roxana Flacau, Mirko Prato, Massimo Colombo, Sergio Marras, Liberato Manna, Stuart Turner, et al. Cation exchange mediated elimination of the fe-antisites in the hydrothermal synthesis of LiFePO_4 . *Nano Energy*, 16:256–267, 2015.
- [30] Sung-Yoon Chung, Si-Young Choi, Takahisa Yamamoto, and Yuichi Ikuhara. Atomic-scale visualization of antisite defects in LiFePO_4 . *Physical review letters*, 100(12):125502, 2008.
- [31] Jiajun Chen, Jianming Bai, Haiyan Chen, and Jason Graetz. In situ hydrothermal synthesis of LiFePO_4 studied by synchrotron x-ray diffraction. *The Journal of Physical Chemistry Letters*, 2(15):1874–1878, 2011.

- [32] Sung-Yoon Chung, Si-Young Choi, Seongsu Lee, and Yuichi Ikuhara. Distinct configurations of antisite defects in ordered metal phosphates: comparison between LiMnPO₄ and LiFePO₄. *Physical review letters*, 108(19):195501, 2012.
- [33] Jiajun Chen and Jason Graetz. Study of antisite defects in hydrothermally prepared LiFePO₄ by in situ x-ray diffraction. *ACS applied materials & interfaces*, 3(5):1380–1384, 2011.
- [34] Kirsten MØ Jensen, Mogens Christensen, Haraldur P Gunnlaugsson, Nina Lock, Espen D Bøjesen, Thomas Proffen, and Bo B Iversen. Defects in hydrothermally synthesized LiFePO₄ and LiFe_{1-x}Mn_xPO₄ cathode materials. *Chemistry of Materials*, 25(11):2282–2290, 2013.
- [35] P Axmann, C Stinner, Margret Wohlfahrt-Mehrens, A Mauger, F Gendron, and CM Julien. Nonstoichiometric LiFePO₄: defects and related properties. *Chemistry of Materials*, 21(8):1636–1644, 2009.
- [36] Robin Amisse, Moulay Tahar Sougrati, Lorenzo Stievano, Carine Davoisne, Goran Drazic, Bojan Budic, Robert Dominko, and Christian Masquelier. Singular structural and electrochemical properties in highly defective LiFePO₄ powders. *Chemistry of materials*, 27(12):4261–4273, 2015.
- [37] Kate Wright and CRA Catlow. A computer simulation study of (oh) defects in olivine. *Physics and Chemistry of Minerals*, 20(7):515–518, 1994.
- [38] GR Rossman. Studies of oh in nominally anhydrous minerals. *Physics and Chemistry of Minerals*, 23(4-5):299–304, 1996.
- [39] John P Brodholt and Keith Refson. An ab initio study of hydrogen in forsterite and a possible mechanism for hydrolytic weakening. *Journal of Geophysical Research: Solid Earth*, 105(B8):18977–18982, 2000.
- [40] Tian Qin, Renata M Wentzcovitch, Koichiro Umemoto, Marc M Hirschmann, and David L Kohlstedt. Ab initio study of water speciation in forsterite: Importance of the entropic effect. *American Mineralogist*, 103(5):692–699, 2018.
- [41] John P Perdew, Kieron Burke, and Matthias Ernzerhof. Generalized gradient approximation made simple. *Physical review letters*, 77(18):3865, 1996.
- [42] Georg Kresse and Jürgen Furthmüller. Efficiency of ab-initio total energy calculations for metals and semiconductors using a plane-wave basis set. *Computational materials science*, 6(1):15–50, 1996.
- [43] <https://github.com/dimonaks/siman/tree/master/siman>.

- [44] Anubhav Jain, Geoffroy Hautier, Charles J Moore, Shyue Ping Ong, Christopher C Fischer, Tim Mueller, Kristin A Persson, and Gerbrand Ceder. A high-throughput infrastructure for density functional theory calculations. *Computational Materials Science*, 50(8):2295–2310, 2011.
- [45] Guohua Li, Hideto Azuma, and Masayuki Tohda. LiMnPO₄ as the cathode for lithium batteries. *Electrochemical and Solid State Letters*, 5(6):A135, 2002.
- [46] Shyue Ping Ong, Lei Wang, Byoungwoo Kang, and Gerbrand Ceder. Li-Fe-P-O₂ phase diagram from first principles calculations. *Chemistry of Materials*, 20(5):1798–1807, 2008.